

¹ Modeling ice-shelf cavities and tabular icebergs using
² Lagrangian elements

A.A. Stern,¹, A. Adcroft¹ and O. Sergienko¹, G. Marques¹, R. Hallberg¹

3 **Key Points:**

4

- 5 • A novel modeling framework is developed to model breakable ice shelves and ice-shelf cavities
6 using Lagrangian elements, held together by numerical bonds.
- 7 • The ocean circulation beneath a (static) Lagrangian ice shelf is almost indistinguishable
8 from the circulation beneath an Eulerian ice-shelf model run in an identical configuration, which
9 provides a proof of concept for the Lagrangian model.
- 10 • After an iceberg calves away from an ice shelf, a complex interaction is observed between
11 the iceberg motion and ocean hydrography. This interaction leads to the formation of a Taylor
12 column beneath the iceberg, a subsurface cooling at the ice front, and reduced melt rates within
13 the ice-shelf cavity.

A. A. Stern, Geophysical Fluid Dynamics Laboratory, Princeton University

A. Adcroft, Geophysical Fluid Dynamics Laboratory, Princeton University

O. Sergienko, Geophysical Fluid Dynamics Laboratory, Princeton University

G. Marques, Geophysical Fluid Dynamics Laboratory, Princeton University

R. Hallberg, Geophysical Fluid Dynamics Laboratory, Princeton University

¹⁴ **Abstract.** The current generation of ice-ocean models is unable to rep-
¹⁵ resent ice-shelf calving in a physically realistic way, despite the controlling
¹⁶ role that calving plays in the setting mass balance and extent of Antarctic
¹⁷ ice shelves. The infrequency of large calving events together with the diffi-
¹⁸ culty of placing observational instruments around tabular icebergs means that
¹⁹ little is known about how calving icebergs affect the ocean. In this study we
²⁰ present a novel model of an ice-shelf cavity below a breakable ice shelf con-
²¹ structed of Lagrangian elements. We validate the Lagrangian ice-shelf model
²² by simulating the flow beneath a (static) idealized ice shelf, and comparing
²³ the results to an Eulerian model simulations with identical configuration. The
²⁴ Lagrangian model is then used to simulate the ocean's response to a tabu-
²⁵ lar iceberg calving away from the ice shelf. The results show how an iceberg
²⁶ calving event and the subsequent iceberg drift affects the ocean conditions
²⁷ at the ice front and around the iceberg. At the ice front, the iceberg calv-
²⁸ ing leads to a warming of the ocean surface and cooling of the water column
²⁹ at depth, allowing cooler waters to enter the ice-shelf cavity. This in turn leads
³⁰ to reduced melt rates within the cavity. A Taylor column is observed below
³¹ the iceberg, which moves with the iceberg as it drifts into the open ocean.
³² As the tabular iceberg drifts further from the ice shelf, the circulation within
³³ the ice-shelf cavity tends towards a new steady state, consistent with the new
³⁴ ice-shelf geometry.

1. Introduction

35 Satellite observations show that ice-shelf decay occurs via two main processes: melting
36 and breaking [Depoorter et al , 2013; Rignot et al , 2013]. Each of these is responsible
37 for approximately half of the ice-shelf decay, and each influences the surrounding ocean
38 (and ice-shelf geometry) in a distinct way. Melting at the base of ice shelves causes fluxes
39 of freshwater into the ice-shelf cavity. The input of buoyant meltwater creates rising density
40 plumes, which are guided along the ice-shelf base, and help drive ocean circulation beneath
41 the ice shelves [MacAyeal , 1984; Holland and Feltham , 2006]. Over time, melting at the
42 ice-shelf base can erode the ice shelf, gradually altering the ice-shelf geometry. In contrast,
43 iceberg calving causes sudden changes to the ice-shelf geometry, and releases giant icebergs
44 into the ocean. After calving, these tabular icebergs can travel large distances and impact
45 ocean hydrography [Martin and Adcroft , 2010; Stern et al , 2015], sea-ice formation
46 [Robinson and Williams , 2012; Stern et al , 2016] and ocean biology [Smith et al , 2007;
47 Vernet et al , 2012; Biddle et al , 2015] many miles away.

48 Modeling the ocean beneath the ice shelves presents a unique set of challenges, since
49 (i) the presence of ice shelves provides a quasi-rigid upper boundary for the ocean model
50 which is not encountered elsewhere in the ocean, and (ii) melting and breaking ice shelves
51 imply changing ocean boundary conditions which present numerous numerical difficulties.

52 The earliest models of ocean ice-shelf cavities were developed using static ice shelves
53 with a fixed shape [Hellmer and Olbers , 1989; Determan and Gerdes , 1994; Grosfeld et
54 al , 1997; Holland and Jenkins , 2001; Losch , 2008]. In these models, ice-shelf melting
55 was represented through salinity and temperature fluxes, while the ice-shelf geometry

56 remained unchanged. Later models of ice-shelf cavities allowed the ice-shelf geometry
57 to evolve as the ice-shelf melted, permitting the study of coupled ocean-ice phenomena
58 [Gladish et al , 2012; Sergienko , 2013]. More recently, dynamic ice-shelf models have
59 been coupled to the ocean cavity, allowing the study of grounding line migration which is
60 of key importance for sea level rise projections [Grosfeld and Sandhger , 2004; Goldberg
61 et al , 2012; De Rydt and Gudmundsson , 2016; Seroussi et al , 2017].

62 All models of ice-shelf cavities to date have omitted ice-shelf breaking and iceberg
63 detachment. This is because (i) there is much uncertainty about the physics that govern
64 ice-shelf breaking [Benn et all , 2007; Alley et al , 2008; Levermann et al , 2012; Bassis
65 and Jacobs , 2013], and (ii) current models of ice-shelf cavities represent the ice shelves on
66 static Eulerian grids, which do not lend themselves to modeling iceberg detachment and
67 drift. In contrast, existing *iceberg* models represent icebergs as Lagrangian particles, since
68 this is a convenient way to model discrete objects traveling over large distances [Bigg et
69 al , 1997; Gladstone et al , 2001; Martin and Adcroft , 2010; Marsh et al , 2015]. To date
70 there has been no real effort to synthesize these two approaches (i.e.: to combine ice shelf
71 and iceberg models).

72 In this study we develop a new ice-shelf cavity model where the ice shelf is simulated
73 with Lagrangian elements [Stern et al , 2017]. In this model, the ice shelf is constructed
74 out of Lagrangian elements which are bonded together by numerical bonds (see schematic
75 Figures 1). This Lagrangian framework allows for large pieces of the ice shelf to break away
76 and become tabular icebergs. An example of this enhanced capability of the Lagrangian
77 model is demonstrated in Figures 2, which shows a tabular iceberg drifting away from an
78 idealized ice shelf.

79 The goals of this study are (i) to introduce and describe the Lagrangian ice-shelf model,
80 (ii) to validate the Lagrangian model by simulating the flow beneath a static idealized
81 ice-shelf cavity, and comparing it to an Eulerian ice-shelf model run in an identical con-
82 figuration, and (iii) to demonstrate the enhanced capabilities of the Lagrangian ice-shelf
83 model by simulating a large iceberg calving away from the idealized ice shelf. Modeling
84 the ocean during and after a calving event, allows us to observe how the calving event
85 affects the ocean near and beneath the ice shelf, and how changes in the ocean feedback
86 onto the ice shelf.

2. Lagrangian model description

87 The Kinematic Iceberg Dynamics (KID) model is a Lagrangian model that has been
88 developed in order to simulate ice-shelf cavities with breakable ice shelves. The model
89 represents ice shelves using Lagrangian elements joined together by numerical bonds. By
90 breaking these bonds, the model is able to simulate ice-shelf calving and iceberg breakup.

91 In this section we describe the Lagrangian ice-shelf model. A more complete description
92 of the model including numerical methods and algorithms used to track the numerical
93 bonds can be found in Stern et al [2017].

2.1. Kinematic Iceberg Dynamics model

94 The KID model is a Lagrangian particle-based model, in that the objects of the model
95 are Lagrangian elements. Each Lagrangian element represents a column of ice that is
96 floating in the ocean. The elements have their own position, velocity, mass, and a set
97 of dimensions, which can evolve in time. Each element moves according to its own mo-
98 mentum balance which is computed in the (Lagrangian) reference frame of the element.

99 The elements experience oceanic, sea ice and atmospheric drag forces, as well as a forces
 100 due to sea surface height gradients, and the Coriolis force [Bigg et al , 1997; Gladstone
 101 et al , 2001; Martin and Adcroft , 2010; Stern et al , 2017]. The elements also interact
 102 with other elements and can be ‘bonded’ together by numerical bonds, which allow many
 103 elements to move together as a unit. By bonding many ice elements together, the model
 104 is able to form larger structures, such as tabular icebergs or ice shelves (Figure 1).

2.2. Equations of motion

The momentum equation for each element is given by

$$M \frac{D\vec{u}}{Dt} = \vec{F}_A + \vec{F}_W + \vec{F}_R + \vec{F}_C + \vec{F}_{SS} + \vec{F}_{SI} + \vec{F}_{IA}, \quad (1)$$

105 where $\frac{D}{Dt}$ is the total (Lagrangian) derivative, M is the mass of the element, \vec{u} is the
 106 velocity of the element, and the terms on the right hand side give the forces on the
 107 element due to air drag (\vec{F}_A), water drag (\vec{F}_W), sea-ice drag (\vec{F}_{SI}), Coriolis force (\vec{F}_C),
 108 wave radiation force (\vec{F}_R), sea surface slope (\vec{F}_{SS}), and interactions with other elements
 109 (\vec{F}_{IA}).

110 The forces on each element are set up such that in the absence of interactive forces,
 111 the ice elements follow the same equations used in iceberg drift models [Bigg et al , 1997;
 112 Gladstone et al , 2001; Martin and Adcroft , 2010]). This ensures that when an element
 113 breaks away from an ice shelf and drifts in the open ocean, it is modeled as a freely drifting
 114 iceberg. When an element is connected to the ice shelf (or larger ice structure), it also
 115 experiences forces due to interactions with the elements around it. The details of these
 116 interactive forces between elements are described below. A complete description of the
 117 other forces acting on the iceberg is provided in Stern et al [2017].

2.3. Interactive Forces

Interactive forces are applied between elements to prevent elements overlapping with neighboring elements, and prevent ‘bonded’ elements from moving apart from one another (see Figures 1a). The interactive forces are modeled as damped elastic forces: For two elements i and j at positions \vec{x}_i and \vec{x}_j , the elastic and damped components of the interactive force are given by

$$(\vec{F}_e)_{ij} = -\kappa_e \left(d_{ij} - L_{ij} \right) M_{ij} \vec{r}_{ij}, \quad (2)$$

and

$$(\vec{F}_d)_{ij} = -M_{ij} c_{r_{||}} P_{\vec{r}_{ij}} \cdot (\vec{u}_i - \vec{u}_j), \quad (3)$$

₁₁₈ respectively. Here $d_{ij} = |\vec{x}_i - \vec{x}_j|$ is the distance between the elements, $\vec{r}_{ij} = \frac{(\vec{x}_i - \vec{x}_j)}{|\vec{x}_i - \vec{x}_j|}$ is the
₁₁₉ directional unit vector between element. L_{ij} is the average diameter of the two elements
₁₂₀ (assuming a circular shape for the elements), κ_e is the spring constant, and M_{ij} is the
₁₂₁ minimum of the masses of elements i and j . $P_{\vec{r}_{ij}}$ is the projection matrix that projects
₁₂₂ onto \vec{r}_{ij} , and $c_{r_{||}}$ is the drag coefficient. We set $c_{r_{||}} = 2\sqrt{\kappa_e}$, so that the elastic force is
₁₂₃ critically damped. The total interactive \vec{F}_{IA} on an element is found by summing up the
₁₂₄ all the interactive forces with other elements.

2.4. Melt rates

₁₂₅ The thickness and extent of the Lagrangian elements change due to melting when they
₁₂₆ are exposed to above-freezing ocean mixed-layer temperatures. The melt rates of the
₁₂₇ elements in the interior of a large structure (such as an ice shelf or large icebergs) are
₁₂₈ parametrized using the three-equation model, which is a typically melt rate parametriza-
₁₂₉ tion used to model basal melt beneath ice shelves [Holland and Jenkins, 1999]. The melt

130 rates of freely floating ice elements (not bonded to other elements) are parametrized us-
131 ing standard parameterizations for iceberg melt [Bigg et al , 1997; Gladstone et al , 2001;
132 Martin and Adcroft , 2010]. For elements at the edge of large structures (with edges partly
133 exposes to the open ocean) the melt rates are computed using a weighted sum of the ice
134 shelf and and iceberg melt rate parametrization, with the weights being proportional to
135 the fraction of the element's perimeter which exposed to the open ocean [Stern et al ,
136 2017].

2.5. Initializing element geometry and packing

137 The elements in the Lagrangian model are shaped as equally-sized regular hexagons (al-
138 though they are treated as circular for the purpose of element interactions). We initialize
139 the Lagrangian model by positioning the elements in a staggered lattice of equally-size
140 hexagons, so that the elements fit together and perfectly tile the ice-shelf surface (Figures
141 1). Hexagonal elements are used so that when adjacent pairs of elements are bonded to-
142 gether, the network of bonds form equilateral triangles, which gives rigidity to the larger
143 structure [Stern et al , 2017]. By using hexagonal elements, which can be packed to-
144 gether without any gaps, the element initialization is perfectly space filling. This allows
145 the model to simulate continuous ice shelves (without gaps or crevasses), and allows the
146 results to be more easily comparable with Eulerian ice-shelf models. In this study, we
147 only use hexagonal elements, however, other element geometries, can be used when less
148 precision is needed.

2.6. Interpolation and aggregation onto the Lagrangian grid

At every time step, ice-shelf fields are passed from the ice-shelf model to the ocean model and from the ocean model to the ice-shelf model. Fields which are passed from the ocean model to the Lagrangian ice-shelf model have to be interpolated from the Eulerian grid onto the Lagrangian grid (i.e.: onto the elements). This is done using a bilinear interpolation scheme. Four ocean fields are passed from the ocean model to the ice-shelf model: temperature, salinity and zonal and meridional velocities.

At the end of an ice-shelf model time step, ice-shelf fields are aggregated from the elements back onto the Eulerian ocean grid, and are then passed from the ice-shelf model to the ocean model. The aggregation from the Lagrangian elements onto the Eulerian grid is done by calculating the fraction of each element's volume that lies in each ocean grid cell, and dividing the fields in proportion to this fraction. For example, the amount of ice mass aggregated onto a given ocean grid cell is found by summing up the masses of all elements which intersect that grid cell, only counting the part of an element's mass that actually intersects the ocean grid cell. When calculating the intersection between an element and a grid cell, we assume that the elements have surface areas that are shaped as regular hexagons. Seven fields are passed from the ice-shelf models to ocean model: iceberg mass and surface area (used to calculate the upper-ocean pressure field), temperature flux, salinity flux and mass flux, and meridian and zonal velocity (used to calculate the momentum flux).

3. Experiment setup

3.1. Domain configuration

In order for our simulations to be easily comparable to previous models of ice-shelf cavities, we use an experimental setup based on the configuration created for the Marine Ice Ocean Modeling Inter-comparison Project (MISOMIP) [Asay-Davis et al , 2016]. The configuration consists of an idealized ice shelf in a rectangular domain $L_x = 80\text{km}$ long and $L_y = 480\text{km}$ wide. The ice shelf is grounded on the southern side of the domain with the ice-shelf front at $y=650\text{km}$. The ice thickness and bottom topography of this setup are shown in Figure 3. The configuration is the same as that of the Ocean0 setup in the MISOMIP, with three changes made:

1. The ‘calving criteria’ used in the MISOMIP study (which states that all points in the ice shelf with thickness less than 100m are set to zero thickness) has not been used.
2. The ice shelf has been thickened on the flanks of the domain, so that the latitude of the grounding line increases away from the center of the ice shelf.
3. The ice shelf is configured to be symmetric about its meridional center line ($x = \frac{L_x}{2}$).

This was achieved by using the average of the left and right flanks of the ice-shelf thickness. These three changes were made in order to make the circulation beneath the ice shelf easier to interpret.

3.2. Ocean model

The Lagrangian and Eulerian ice shelves are coupled to the MOM6 ocean model [Hallberg et al , 2013]. The ocean model is run using a hybrid vertical coordinate system which blends a sigma-level and a z-level coordinate [Stern et al , 2017], implemented using the ALE method [White et al , 2009]. In this vertical coordinate, model layers bend

underneath surface topography (i.e.: the ice shelf), as they would in a sigma coordinate model, and intersect the bottom topography, as they would in a z-coordinate model. The model has 72 vertical layers and has a horizontal resolution of $\Delta x = 2$ km. The numerical simulations were all repeated using an isopycnal coordinate (without ALE regridding-remapping). The results were qualitatively similar to the hybrid-coordinate results, and are therefore not presented here.

The ocean parameters used in the simulations are as specified in the MISOMIP configuration [Asay-Davis et al , 2016], and are shown in Table 1. The simulation is initialized from rest, with horizontally uniform initial ocean temperature and salinity profiles which vary linearly between specified open-ocean surface and bottom values: $T_{top} = -1.9^{\circ}\text{C}$, $T_{bottom} = 1.0^{\circ}\text{C}$, $S_{top} = 33.8$ psu, $S_{bottom} = 34.7$. The maximum ocean depth is $H_{ocean} = 720$ m. A sponge layer is used on the northern boundary, which relaxes back to the initial temperature and salinity with a relaxation time scale of $T_{sponge} = 0.1$ days over a distance of 10 km. Melting is set to zero for ocean cells where the ocean column thickness is less than 10m.

3.3. Lagrangian ice-shelf model:

The Lagrangian ice-shelf simulations are performed using the Kinematic Iceberg Dynamics (KID) model described in Section 2. The Lagrangian ice shelf is created using 10882 Lagrangian hexagonal elements with sides of length $S = 0.98$ km . The positions of the hexagonal elements are initialized by packing them together in a space-filling staggered lattice. Gaps along the boundaries are filled in using smaller elements so that the total ice-shelf area is preserved. The initial mass of the ice elements is determined using bilinear interpolation from a prescribed gridded ice mass field.

3.4. Eulerian ice-shelf model:

210 The Eulerian ice-shelf simulation is performed using an existing Eulerian ice-shelf cavity
 211 model [Goldberg et al , 2012], which is an optional module of the the MOM6 ocean model.
 212 The ice shelf is initialized on the same grid as the ocean model with a horizontal resolution
 213 of $\Delta x = 2$ km. The ice-shelf thickness field is initialized using the same ice-shelf draft used
 214 for the Lagrangian model (Figure 3). The melt rates in the Eulerian ice-shelf simulation
 215 are calculated using the 3 equation model for ice-shelf decay [Holland and Jenkins, 1999],
 216 with the same parameters used to calculate the ice-shelf melt rates in the Lagrangian
 217 model.

4. Model validation

218 The Lagrangian ice-shelf model is validated by comparing it to an existing Eularian
 219 ice-shelf model in an identical static configuration.

4.1. Setup of static validation experiment:

220 The experimental setup for the model validation experiment is based on the Ocean0
 221 MISOMIP experiment [Asay-Davis et al , 2016]. In this experiment the ice shelves are
 222 thermodynamically active but have a time-invariant thickness. Temperature and salinity
 223 fluxes from ice-shelf melt drive the circulation within the cavity.

224 A constant wind stress $\vec{\tau} = \langle \tau_x, \tau_y \rangle = \langle 0.05, 0.05 \rangle \frac{N}{m^2}$ is applied to the ocean surface.

225 Note that this wind stress is was not applied in the original MISOMIP experiments [Asay-
 226 Davis et al , 2016].

227 The elements in the Lagrangian ice shelf simulation are held stationary so that the ice
228 shelf is static and comparable to the Eulerian simulation. The models are spun up for 5
229 years. The analysis is performed on year 6 to 10 of the simulations.

4.2. Results of validation experiment

230 The results of the static ice shelf simulations in both simulations are qualitatively similar
231 to results presented in [Asay-Davis et al , 2016]. Melting at the base of the ice shelf drives
232 a circulation within the cavity and strong jets are observed at the ice front and along the
233 sides of the domain (Figure 4). A more complete description of the circulation is provided
234 in the supplementary material.

235 Since the Lagrangian and Eulerian ice-shelf models are coupled to the same ocean model
236 and the ice-shelf models use the same parametrization for ice-shelf melt, we expect the
237 results of the two models to be the almost the same, with the only differences arising from
238 the interpolation and aggregation schemes (see Section 2.6). The results show that two
239 simulations are almost indistinguishable. This is demonstrated, for example, in Figure
240 4, which shows the time-averaged barotropic stream function of the Lagrangian (Figures
241 4a) and Eulerian (Figures 4b) simulations, and the difference between the two (Figures
242 4c). The difference between the Lagrangian and Eulerian barotropic stream functions are
243 two orders of magnitude smaller than typical differences observed between simulations
244 using different models in the Ocean0 MISOMIP experiment [Asay-Davis et al , 2016].
245 The similarity of the Lagrangian and Eulerian simulations are also reflected in the fact
246 that the simulations have very similar ice-shelf melt rates and ocean temperature/salinity
247 profiles (shown in Figures S1 and S2 in the supplementary materials).

248 The agreement between the Eulerian and Lagrangian simulations is a confirmation that
249 the Lagrangian model is able to simulate sub-ice-shelf cavities as well as the Eulerian
250 model does. This is a good starting point for moving beyond the capabilities of the
251 Eulerian model.

5. Iceberg calving experiment

252 The infrequency of large calving events together with the difficulty of placing observa-
253 tional instruments around tabular icebergs means that little is known about how calving
254 icebergs affect ocean circulation around the iceberg and at the ice front. The Lagrangian
255 ice-shelf model developed in this study allows us for the first time to simulate an iceberg
256 calving away from the ice shelf, and to study what effect this has on the ocean around the
257 iceberg and beneath the ice shelf. Since the Lagrangian iceberg/ice-shelf model is fully
258 coupled to the ocean, the iceberg motion affects the ocean hydrography, and the changing
259 ocean conditions feedback onto the ice.

260 In this section, the Lagrangian ice-shelf model is used to simulate a tabular iceberg
261 detaching from the ice shelf, and drifting into the open ocean. The results below show
262 that the calving of a large tabular iceberg can cause significant changes to the ocean
263 stratification and circulation around the iceberg and at the ice shelf front.

5.1. Setup of iceberg calving experiment:

264 The iceberg calving experiment is initialized using the final state of the static Lagrangian
265 ice shelf simulation (i.e.: at time $t = 10$ years). When initializing the calving event, we
266 bypass the question of how to prescribe a physical calving law [Benn et all , 2007; Alley
267 et al , 2008; Levermann et al , 2012; Bassis and Jacobs , 2013] by manually breaking off

268 a semi-circular iceberg. All ice elements initially within a 14.4 km radius of the center
269 of the ice front are allowed to move freely while the other ice elements continue to be
270 held stationary. Ice elements less than 12 km from the center of the ice front, are bonded
271 together to form a semi-circular tabular iceberg. A ring of elements whose distance, d ,
272 from the ice front center obeys $12 \text{ km} \leq d \leq 14.4 \text{ km}$, are allowed to move freely, but
273 have all their bonds removed.

5.2. Results of iceberg calving experiment

274 5.2.1. Ocean response to iceberg detachment

275 After the numerical bonds are broken, a large semi-circular tabular iceberg detaches
276 from the ice shelf, and begins to drift northwards (Figure 2). The detachment of the
277 iceberg gives rise to a dynamical ocean response which is shown in the schematic in
278 Figure 5a and 5b, and is described below.

279 Immediately after calving, the northwards motion of the iceberg creates a region of open
280 water at the new calving front, between the ice shelf and the tabular iceberg (Figure 2a).
281 The formation of a region of open ocean behind the iceberg causes a sudden stretching of
282 the water column in the wake of the iceberg, which drives an upwelling throughout the
283 water column. The negative background temperature gradient (cold over warm) means
284 that this upwelling is observed as warm water anomaly beneath newly formed ice front
285 (Figure 6a and 7a). The warming is observed throughout the water column, but is largest
286 near the surface. Similarly, the upwelling leads to increased salinity beneath newly formed
287 ice front (not shown).

288 The calving event also drives an immediate change in ocean currents at the newly
289 created ice front as the ocean adjusts to the topographic changes. Since the Coriolis

parameter is negative, a stretching of the water column behind the iceberg has to be accompanied by the creation of negative relative vorticity in order for potential vorticity (PV) to be conserved. The creation of negative relative vorticity along the newly calved ice front, gives rise to a pair of oppositely orientated ocean jets running along the ice front. A westward barotropic jet is created to the south of the calving front, and an eastward barotropic jet is created to the north of the calving front (Figures 8a and 9). The positive gradient in zonal velocity created by this pair of oppositely orientated jets yields the negative relative vorticity, needed to conserve PV.

To the north of the iceberg, the iceberg detachment has the opposite effect on the ocean. The forward movement of the iceberg causes a squeezing of the water column directly in front of the iceberg. This shortening of the water column causes a downwelling in the water column in front of the iceberg, which is observed as a cool water anomaly in front of the iceberg (Figure 6a). The squeezing of the water column generates positive relative vorticity, so that the total PV is conserved. The positive relative vorticity creates an eastward and westward jet to the south and north of the northern edge of the iceberg (Figures 8a and 9). The stretching and squeezing of the water column to the south and north of the iceberg, both contribute to the eastward jet which forms directly beneath the iceberg which plays an important role in driving iceberg motion.

(If you have time, check whether when the wind goes in the other direction, the jet beneath the iceberg moves in the other direction.)

5.2.2. Iceberg motion

After the iceberg breaks away from the ice shelf, the motion of iceberg is primarily driven by the drag from ocean currents beneath the iceberg, wind drag and by Coriolis

313 force. The eastward jet beneath the iceberg drives the iceberg towards the east (Figures
314 8a and 9), while the wind and Coriolis force drive the iceberg offshore. Initially, as the
315 iceberg drifts eastward, it collides with the ice shelf, which hinders its motion (Figure 2a).
316 Only once the iceberg has drifted sufficiently far northwards to be clear of the ice shelf,
317 does it begin to drift towards the east. Once this happens, the iceberg velocity quickly
318 adjusts so that it is approximately equal to the ocean velocity below the iceberg. As the
319 iceberg drifts northwards, it rotates in a counter-clockwise direction (Figure 2).

320 The motion of the iceberg plays a large role in setting the direction of the ocean flow
321 below and around the iceberg, since the ocean has to adjust to topographical changes so
322 that PV is conserved. This is illustrated, for example, by the change in orientation of
323 the ocean jets running beneath the iceberg that occurs as the iceberg rotates (Figure 8b).

324 An important consequence of the controlling effect of iceberg topography is formation of
325 a Taylor Column below the iceberg: the water column below the iceberg is constrained
326 to move at the same speed as the iceberg above, since differential motion would force
327 the water column out from under the iceberg, causing the water column to stretch, and
328 generating PV. This means that the column of water beneath the iceberg is largely sep-
329 arated from the water around the iceberg and strong gradients in temperature, salinity
330 and velocity can exist at the iceberg edge. In our experiment, a Taylor Column is clearly
331 observed below the iceberg throughout the simulation (Figure 10).

332 Once the iceberg reaches the eastern side of the domain, it begins to interact the bound-
333 ary of the domain and with the southward boundary current running along the edge of
334 the domain (Figures 2b and 11c). The presence of the iceberg along the eastern boundary
335 impedes the southward boundary current, so that the current has to flow to the west of

336 the iceberg (Figure 11c). The diverted current follows the topographic contour created by
337 the iceberg so that it sets up a counter-clockwise circulation running around the iceberg
338 (Figure 8c). The eastward jet which was previously positioned beneath the iceberg shifts
339 to the south and becomes part of the flow directing the boundary current around the ice-
340 berg. This counter-clockwise circulation around the iceberg remains around the iceberg
341 until the end of the simulation. Interestingly, the iceberg continues to move northward
342 despite the fact that it is moving within a southward flowing boundary current (Figure
343 10b). This is partly due to the Taylor Column beneath the iceberg, which allows the
344 northward velocity beneath the iceberg to be separated from the southward moving cur-
345 rent around the iceberg. The rotation of the iceberg and interaction with the boundary
346 current are summarized in the schematics in Figure 5c and 5e.

347 **5.2.3. Surface warming and sub-surface cooling**

348 After the tabular iceberg detaches from the ice shelf, a warming is observed throughout
349 the water column to the south of the iceberg (Figure 6a, as discussed above). This warming
350 extends to the ocean surface, resulting in warm sea surface temperature (SST) anomalies
351 at the newly calved ice front and around the southern side of the iceberg (Figure 2 and
352 7a). In the weeks following calving, part of this warm SST anomaly remains at the ice
353 front, influencing the heat flux into the ice-shelf cavity, and some the SST anomaly drifts
354 with the iceberg into the open ocean.

355 The warm SST anomalies at the ice front persist and strengthen, even once the tabular
356 iceberg has drifted away, as water continues to upwell at the newly formed ice front. Some
357 of this warmed surface water is advected to west by the westward jet at the ice front (Figure
358 2c). Once these warmed surface waters reach the western side of the domain, most of this

³⁵⁹ warm anomaly is advected northwards following the western boundary, while some of the
³⁶⁰ warmth is forced southward, and is able to subduct beneath ice shelf on the western side
³⁶¹ of the ice shelf front.

³⁶² The SST anomalies that drift along with the iceberg are initially concentrated along
³⁶³ the curved southern side of the iceberg. As the tabular iceberg drifts away from the ice
³⁶⁴ shelf (and begins to rotate), the currents that develop around the iceberg advect this
³⁶⁵ warm SST anomaly counter-clockwise around the perimeter of the iceberg so that by 15
³⁶⁶ days after calving, the SST around the most of the iceberg's perimeter is anomalously
³⁶⁷ warm (Figure 2). As the iceberg drifts further into the open ocean, the warmed surface
³⁶⁸ waters around the iceberg's perimeter mix with the ambient surface water, leaving a trail
³⁶⁹ of warmed surface water which maps out the wake of the iceberg. It is likely that as
³⁷⁰ the iceberg drifts, the motion of the iceberg and strong sheer in horizontal velocity at
³⁷¹ the iceberg edges contribute to continued upwelling, leading to further increased surface
³⁷² warming.

³⁷³ As discussed above, the downwelling on the northern side of the iceberg observed im-
³⁷⁴ mediately after calving, leads to a cooling/freshening of the water column beneath and to
³⁷⁵ the north of the iceberg (Figure 6 and 7). As the iceberg drifts away from the ice shelf,
³⁷⁶ the cool water anomalies remain beneath the iceberg, traveling with the iceberg into the
³⁷⁷ open ocean, leaving a trail of cool subsurface temperature anomalies which maps out the
³⁷⁸ (subsurface) wake of the iceberg (not shown). The pattern of warm surface anomalies
³⁷⁹ around the iceberg, and cool subsurface anomalies around the iceberg, is clearly visible
³⁸⁰ throughout the simulation (Figure 10c), and suggests continued vertical mixing around
³⁸¹ the iceberg perimeter as it drifts into the open ocean.

382 About 5 days after calving, as the iceberg begins to rotate counter clockwise, the jet
383 to the north of the iceberg begins to drive the cool water anomaly towards the ice front
384 (Figure 8b). The strong jet moving towards the ice front causes water to subduct beneath
385 the ice front, leading to further cool sub-surface anomalies. Below the depth of the
386 ice shelf, the cool water anomalies are stronger than the warm water anomalies caused
387 by the initial water column stretching. The subsurface negative temperature anomalies
388 strengthen over time and within a month of the calving event, the negative anomalies
389 occupy most of the water column close to the ice front (Figure 7). This subsurface cooling
390 at the ice front is the most prominent temperature response observed in our iceberg calving
391 experiments. Similar subsurface cooling at the ice front was observed in other experiments
392 using different sizes and shapes for the calving iceberg (not shown). The sub-subsurface
393 cooling and warm surface temperature anomalies discussed above are accompanied by a
394 freshening at depth and increase in surface salinity (not shown).

395 The zonal current along the ice front drives the cool anomaly to the west, causing an
396 enhancement of the cool anomalies on the western side of the ice shelf front (Figure 7c).
397 Most of the subsurface cooling occurs outside of the ice-shelf cavity, as the dynamical
398 barrier caused by the ice shelf inhibits exchange of water across the ice front. However
399 over time, an increasing amount of cooler water is able to enter the ice-shelf cavity, and
400 is advected below the ice shelf (Figure 6c).

401 The surface warming at the ice front and around the iceberg, as well as the subsurface
402 cooling at the ice front, are summarized in the schematics in Figure 5c, 5d and 5e.

403 **5.2.4. Inside the ice-shelf cavity**

404 The combination of cool sub-surface temperature anomalies and elevated ocean veloci-
405 ties at the ice front, results in a temperature flux across the ice front, as cool temperature
406 anomalies to enter the ice-shelf cavity (Figure 6, Figure 5f). Once the cooler water has
407 entered the ice-shelf cavity, the anomalies spread southwards within the ice-shelf cavity,
408 eventually reaching all the way to the grounding line. As the cool water spreads into
409 the cavity, it mixes with the water within the ice-shelf cavity, causing a reduction in the
410 strength of the anomaly towards the grounding line (Figure 6c).

411 The cooling of the water inside the ice-shelf cavity after calving leads to a reduction of
412 the melt rates at the base of the ice shelf (Figure 12). The reduced melt rates occur over
413 a wide area extending from the newly calved ice front, all the way towards the grounding
414 line. The negative melt rate anomalies increase over time, as more cold water enters the
415 ice-shelf cavity. The strongest negative anomalies are observed near the ice front, while
416 the strength of the negative melt rate anomalies are reduced towards the grounding. The
417 reduction in melt rates are up to 0.5 m per year, which is small compared to the mean
418 melt rates near the grounding line, but is a substantial fraction of the melt at intermediate
419 depths (Figure S4a).

420 Near the ice front, the competing effects of warm surface water subducting beneath the
421 ice shelf on the flanks of the domain, and the cool water entering the ice shelf in the enter
422 of the domain, lead to a complex of pattern of positive and negative melt rate anomalies
423 within 20 km of the ice front (Figure 12).

424 **5.2.5. Equilibrium hydrography**

425 The presence of a northern boundary in our simulation mean that we are unable to
426 entirely remove the iceberg from the domain and observe the system approaching a new

equilibrium state. However, a comparison between the iceberg-calving simulation and an ‘equilibrium-shelf simulation’ (where the model was spun up with the iceberg removed from the start), shows that after 60 days the hydrography inside the ice-shelf cavity in the iceberg-calving simulation appears to be qualitatively similar to equilibrium-shelf simulation steady state (see Figure S5 in the supplementary material, for example). This suggests that the processes occurring at the ice front directly after calving are transient processes which allow the system to move towards a steady state that is largely controlled by the ice-shelf geometry. Since the ice-shelf geometry in our simulation is highly idealized and is in a closed domain, it is unclear whether the adjustment time scale seen here is relevant to real-world ice shelves.

6. Summary

The simulations presented above demonstrate that the calving of a large tabular iceberg can cause significant changes to the ocean stratification and circulation around the iceberg and at the ice front. Although the idealized geometry of the simulations makes it difficult to compare the results directly to real-world observations, a number of robust features were observed in this iceberg-calving simulation, which could have real-world analogues.

1. Dynamical response of ocean to iceberg calving:

As the iceberg detaches from the ice shelf, there is an immediate dynamical ocean response: a stretching of the water column directly behind the iceberg gives rise to ocean upwelling, which leads to a warm salty anomalies being created at the newly calved ice front. PV conservation implies that this ocean column stretching gives rise to the formation of pairs of oppositely orientated jets which form directly behind the iceberg. A similar (and oppositely signed) phenomenon occurs in front of the iceberg, where a squeezing of the water column

449 leads to downwelling, a cooling/freshening of the water column and a pair of oppositely
450 orientated jets being created along the front side of the iceberg (see schematic in Figure
451 5a, 5b).

452 **2. Controlling influence of iceberg topography:**

453 The iceberg topography has a controlling affect on the ocean below it. This is demon-
454 strated by the shifting of ocean jets below the iceberg in response to the iceberg motion. It
455 is also demonstrated by the Taylor forms directly below the iceberg. This Taylor column
456 follows the iceberg as it drifts into the open ocean and leads to a separation between the
457 ocean properties below the iceberg and the ambient ocean conditions.

458 **3. Localized changes in ocean hydrography around the iceberg:**

459 The calving and motion of the iceberg has a large and complex affect on ocean temperate
460 and salinity around the iceberg and at the calving front. In our experiment, warmed water
461 surrounds the iceberg as it drift away from the ice shelf and maps out a trail of warm
462 surface anomalies in the wake of the iceberg. Similarly, cooler waters are observed below
463 the iceberg and map out a trail of cool sub-surface anomalies in the iceberg wake.

464 **4. Interaction between iceberg and ocean currents:**

465 As the iceberg drifts away form the ice shelf, it interacts with the ocean current coming
466 towards the ice shelf. The iceberg impedes the ocean current which is diverted around the
467 iceberg and sets up a new circulation around the iceberg. In our simulation, the change in
468 circulation directs a current towards the center of the ice shelf front. This water subduct
469 causing large cool anomalies at the ice front (see schematic in Figure 5).

470 **5. Iceberg calving can affect sub-ice shelf temperatures and melt rates:**

471 Large changes in ocean properties which occur at the ice front following the iceberg calving

472 can directly affect the temperature flux into the ice-shelf cavity, which in turn alter the
473 sub-ice-shelf melt rates. In our experiment, the cool water subducting beneath the ice
474 shelf lead to reduced melt rates beneath the ice shelf. This decrease in melt rate extends
475 far into the ice-shelf cavity.

476 **6. Controlling influence of the ice-shelf geometry:**

477 Once the iceberg has drifted far away from the ice-shelf cavity, the conditions and melt
478 rates within the ice-shelf cavity appear to be converge towards values similar to those
479 in simulations run with the iceberg removed from the start. This result suggests that
480 the melt rates inside the ice-shelf cavity are largely controlled by the ice-shelf geometry.
481 The changes in ocean conditions caused by the interaction with the iceberg appear to be
482 transient adjustment processes.

7. Conclusion

483 This study presents a new Lagrangian framework for modeling sub-ice-shelf cavities. In
484 this framework, the ice shelf is constructed out of many Lagrangian elements, which are
485 bonded together by numerical bonds.

486 By breaking the bonds, we can use the Lagrangian model to simulate iceberg calving,
487 and to observed the ocean response to large calving events (Figures 2). This capability is
488 currently not possible using more traditional Eulerian models [Stern et al , 2017].

489 We validate the Lagrangian ice-shelf model by simulating the flow beneath a (static)
490 idealized ice shelf, and comparing the results to an existing Eulerian model simulation
491 with identical configuration. This comparison show that the results from Lagrangian
492 and Eularian models are almost indistinguishable. This agreement confirms that the
493 Lagrangian model is able to simulate sub-ice-shelf cavities as well as the Eulerian model.

⁴⁹⁴ Demonstrating that the Lagrangian ice-shelf model is able to reproduce the results of
⁴⁹⁵ an Eulerian ice-shelf model in the same static ice-shelf configuration is a prerequisite
⁴⁹⁶ developing more advanced Lagrangian models and represents a good benchmark test for
⁴⁹⁷ new Lagrangian ice-shelf models.

⁴⁹⁸ The Lagrangian ice shelf model is then used to simulate a tabular iceberg calving away
⁴⁹⁹ from an ice shelf. The results from this experiment demonstrate the complex interaction
⁵⁰⁰ between a calving iceberg and the surrounding ocean, and suggests that iceberg-ocean
⁵⁰¹ interactions can significantly affect ocean currents and hydrography around calving sites,
⁵⁰² and can even feedback onto melt rates within the ice-shelf cavity. More work is needed
⁵⁰³ to further understand these iceberg-ocean interactions, and to gauge how these dynamics
⁵⁰⁴ might affect real-world ice shelf cavities. The Lagrangian ice-shelf model presented in this
⁵⁰⁵ study could be a useful tool to study these interactions using both idealized and real-world
⁵⁰⁶ geometries.

References

- 507 Asay-Davis, X. S., S. L. Cornford, B. K. Galton-Fenzi, R. M. Gladstone, G. H. Gudmundsson, D. M. Holland, P. R. Holland, and D. F. Martin (2016), Experimental design for
508 three interrelated marine ice sheet and ocean model intercomparison projects: MIS-
509 MIP v. 3 (MISMIP+), ISOMIP v. 2 (ISOMIP+) and MISOMIP v. 1 (MISOMIP1).
510 *Geoscientific Model Development* 9, no. 7: 2471.
- 511
- 512 Arrigo, K. R., G. L. van Dijken, D. G. Ainley, M. A. Fahnestock, and T. Markus (2002).
513 Ecological impact of a large Antarctic iceberg. *Geophys. Res. Lett.*, 29(7).
- 514 Alley, R. B., H. J. Horgan, I. Joughin, K. M. Cuffey, T. K. Dupont, B. R. Parizek, S.
515 Anandakrishnan, and J. Bassis (2008), A simple law for ice-shelf calving. *Science* 322,
516 no. 5906, 1344-1344.
- 517 Bassis, J. N., and S. Jacobs (2013), Diverse calving patterns linked to glacier geometry.
518 *Nature Geoscience*, 6(10), 833-836.
- 519 Benn, D. I., C. R. Warren, and R. H. Mottram (2007). Calving processes and the dynamics
520 of calving glaciers. *Earth-Science Reviews*, 82(3), 143-179.
- 521 Bigg, G. R., Wadley, M. R., Stevens, D. P., and Johnson, J. A. (1997), Modeling the
522 dynamics and thermodynamics of icebergs. *Cold Regions Science and Technology*, 26(2),
523 113-135.
- 524 Borstad, C. P., A. Khazendar, E. Larour, M. Morlighem, E. Rignot, M. P. Schodlok, and
525 H. Seroussi (2012), A damage mechanics assessment of the Larsen B ice shelf prior to
526 collapse: Toward a physically-based calving law, *Geophys. Res. Lett.*, 39, L18502
- 527 Biddle, L. C., J. Kaiser, K. J. Heywood, A. F. Thompson and A. Jenkins (2015), Ocean
528 glider observations of iceberg-enhanced biological productivity in the northwestern Wed-

- 529 dell Sea, *Geophys. Res. Lett.*, 42, 459465.
- 530 De Rydt, J., and G. H. Gudmundsson (2016), Coupled ice shelf ocean modeling and
531 complex grounding line retreat from a seabed ridge. *J. of Geophys. Res.: Earth Surface*,
532 121(5), 865-880.
- 533 Dunne, J.P., J.G. John,, A.J. Adcroft, S.M. Griffies, R.W. Hallberg, E. Shevliakova,
534 R.J. Stouffer, W. Cooke, K.A. Dunne, M.J Harrison, and J.P. Krasting (2012), GFDL's
535 ESM2 global coupled climate-carbon Earth System Models. Part I: Physical formulation
536 and baseline simulation characteristics. *J. of Climate*, 25(19), 6646-6665.
- 537 Depoorter, M. A., J. L. Bamber, J. A. Griggs, J. T. M. Lenaerts, Stefan RM Ligtenberg,
538 M. R. van den Broek, and G. Moholdt (2013), Calving fluxes and basal melt rates of
539 Antarctic ice shelves. *Nature*, 502(7469), 89-92.
- 540 Determan J., Gerdes R. (1994), Melting and freezing beneath ice shelves: implications
541 from a three-dimensional ocean-circulation model. *Ann. Glaciol.*, 20, 413-419.
- 542 Dowdeswell, J. A., and J. L. Bamber (2007), Keel depths of modern Antarctic icebergs
543 and implications for sea-floor scouring in the geological record. *Marine Geology*, 243(1),
544 120-131.
- 545 Duprat, L. P., G. R. Bigg, and D. J. Wilton (2016), Enhanced Southern Ocean marine
546 productivity due to fertilization by giant icebergs. *Nature Geoscience*.
- 547 Eckert, E. R. G. (1950). Introduction to the Transfer of Heat and Mass. McGraw-Hill.
- 548 Gladstone, R. M., G. R. Bigg, and K. W. Nicholls. (2001), Iceberg trajectory modeling
549 and meltwater injection in the Southern Ocean (19782012). *J. of Geophys. Res.: Oceans*,
550 106(C9), 19903-19915.

- 551 Goldberg, D. N., C. M. Little, O. V. Sergienko, A. Gnanadesikan, R. Hallberg, and M.
552 Oppenheimer (2012), Investigation of land ice?ocean interaction with a fully coupled
553 ice-ocean model: 1. Model description and behavior. *J. of Geophys. Res.: Earth Surface*,
554 117(F2).
- 555 Gladish, C. V., D. M. Holland, P. R. Holland, and S. F. Price (2012), Ice-shelf basal
556 channels in a coupled ice/ocean model. *J. of Glaciol.*, 58(212), 1227-1244.
- 557 Grosfeld K., R. Gerdes, J. Determan (1997), Thermohaline circulation and interaction
558 between ice shelf cavities and the adjacent open ocean. *J. Phys. Oceanogr.*, **102**, C7,
559 15959-15610.
- 560 Grosfeld, K., and H. Sandhger, (2004). The evolution of a coupled ice shelfocean system
561 under different climate states. *Global and Planetary Change*, 42(1), 107-132.
- 562 Hallberg, R., A. Adcroft, J. P. Dunne, J. P., Krasting, R. J., and Stouffer (2013), Sensitiv-
563 ity of twenty-first-century global-mean steric sea level rise to ocean model formulation.
564 *J. of Climate*, 26(9), 2947-2956.
- 565 Holland D. M., Jenkins A. (2001), Adaptation of an isopycnic coordinate ocean model for
566 the study of circulation beneath ice shelves. *Mon. Wea. Rev.*, 129, 1905-1927.
- 567 Holland P. R. and D. L. Feltham (2006), The effects of rotation and ice shelf topography
568 on frazil-laden Ice Shelf Water plumes. *J. Phys. Oceanogr.*, 36, 2312-2327.
- 569 Holland, D. M., and A. Jenkins (1999), Modeling thermodynamic ice-ocean interactions
570 at the base of an ice shelf. *J. of Phys. Oceanogr.* 29.8, 1787-1800.
- 571 Hellmer H.H., Olbers D. J. (1989), A two-dimensional model for the thermohaline circu-
572 lation under an ice shelf. *Antarctic Science*, 1, 325- 336.

- 573 Hopkins, M. A. (1996). On the mesoscale interaction of lead ice and floes. *J. of Geophys. Res.: Oceans*, 101(C8), 18315-18326.
- 575 Jakobsen, T. (2001). Advanced character physics. In *Game Developers Conference*, Vol. 3.
- 577 Jenkins, A., P. Dutrieux, S. S. Jacobs, S. D. McPhail, J. R. Perrett, A. T. Webb, and
578 D. White (2010), Observations beneath Pine Island Glacier in West Antarctica and
579 implications for its retreat. *it Nature Geo.*, 3(7), 468-472.
- 580 Jacobs, S. S., A. Jenkins, C. F. Giulivi, and P. Dutrieux (2011). Stronger ocean circulation
581 and increased melting under Pine Island Glacier ice shelf. *Nature Geo.*, 4(8), 519-523.
- 582 Jongma, J. I., E. Driesschaert, T. Fichefet, H. Goosse, and H. Renssen (2009), The effect of
583 dynamic-thermodynamic icebergs on the Southern Ocean climate in a three-dimensional
584 model, *Ocean Modell.*, 26, 104113.
- 585 Lewis E.L. and R.G. Perkin (1986), Ice pumps and their rates. *J. of Geophys. Res.*, 91,
586 11756-11762.
- 587 Losch, M. (2008). Modeling ice shelf cavities in az coordinate ocean general circulation
588 model. *J. of Geophys. Res.: Oceans*, 113(C8).
- 589 Li, B., H. Li, Y. Liu, A. Wang and S. Ji (2014), A modified discrete element model for
590 sea ice dynamics. *Acta Oceanologica Sinica*, 33(1), 56-63.
- 591 Liu, M. B. and G. R. Liu (2010), Smoothed particle hydrodynamics (SPH): an overview
592 and recent developments. *Archives of computational methods in engineering*, 17(1), 25-
593 76.
- 594 Lichy, C., and H. H. Hellmer (2001). Modeling giant-iceberg drift under the influence of
595 sea ice in the Weddell Sea, Antarctica. *J. of Glaciol.*, 47(158), 452-460.

- 596 Levermann, A., T. Albrecht, R. Winkelmann, M. A. Martin, M. Haseloff, and I. Joughin.
597 (2012), Kinematic first-order calving law implies potential for abrupt ice-shelf retreat.
598 *The Cryosphere*, 6(2), 273-286.
- 599 Martin, T., and Adcroft, A. (2010), Parameterizing the fresh-water flux from land ice
600 to ocean with interactive icebergs in a coupled climate model. *Ocean Modelling*, 34(3),
601 111-124.
- 602 Marsh, R., V. O. Ivchenko, N. Skliris, S. Alderson, G. R. Bigg, G. Madec, A. T. Blaker
603 Y. Aksenov, B. Sinha, A.C. Coward, and J.L. Sommer (2015), NEMOICB (v1. 0):
604 interactive icebergs in the NEMO ocean model globally configured at eddy-permitting
605 resolution. *Geoscientific Model Development* 8, no. 5 (2015): 1547-1562.
- 606 MacAyeal D.R. (1984), Thermohaline Circulation Below the Ross Ice Shelf: A Conse-
607 quence of Tidally Induced Vertical Mixing and Basal Melting. *J. Geophys. Res.*, 89,
608 597-606
- 609 Nicholls K.W. (1996), Temperature variability beneath Ronne Ice Shelf, Antarctica, from
610 thermistor cables. *J. Phys. Oceanogr.*, 11, 1199-1210.
- 611 Nicholls KW, Østerhus S, Makinson K (2009), Ice-Ocean processes over the continental
612 shelf of the southern Weddell Sea, Antarctica: a review. *Rev. Geophys.* 47(3).
- 613 Omelyan, I. P., M. I. Mryglod, and R. Folk (2002), Optimized Verlet-like algorithms for
614 molecular dynamics simulations. *Physical Review E*, 65(5), 056706.
- 615 Rignot, E., S. Jacobs, J. Mouginot, and B. Scheuchl (2013), Ice-shelf melting around
616 Antarctica. *Science*, 341, no. 6143 (2013): 266-270.
- 617 Robinson, N. J., and Williams, M. J. M. (2012). Iceberg-induced changes to polynya
618 operation and regional oceanography in the southern Ross Sea, Antarctica, from in situ

- 619 observations. *Antarctic Science*, 24(5), 514-526.
- 620 Pan, W., A. M. Tartakovsky, and J. J. Monaghan (2013). Smoothed particle hydrody-
621 namics non-Newtonian model for ice-sheet and ice-shelf dynamics. *J. of Comp. Phys.*,
622 242, 828-842.
- 623 Pralong, A., and M. Funk (2005), Dynamic damage model of crevasse opening and appli-
624 cation to glacier calving, *J. Geophys. Res.*, 110, B01309.
- 625 Seroussi H., Y. Nakayama, E.Y. Larour, D. Menemenlis, M. Morlighem, E. Rignot, and A.
626 Khazendar (2017), Continued retreat of Thwaites Glacier, West Antarctica, controlled
627 by bed topography and ocean circulation, *Geophys. Res. Lett.*, 44
- 628 Sergienko, O. V. (2013). Basal channels on ice shelves. *J. of Geophys. Res.: Earth Surface*,
629 118(3), 1342-1355.
- 630 Silva, T. A. M., Bigg, G. R., and Nicholls, K. W. (2006), Contribution of giant icebergs
631 to the Southern Ocean freshwater flux. *J. of Geophys. Res.: Oceans*, 111(C3).
- 632 Smith, K., B. Robison, J. Helly, R. Kaufmann, H. Ruhl, H., T. Shaw, and M. Vernet
633 (2007), Free-drifting icebergs: Hotspots of chemical and biological enrichment in the
634 Weddell Sea, *Science*, 317, 478482.
- 635 Stern, A. A., D. M. Holland, P. R. Holland, A. Jenkins and J. Sommeria (2014), The effect
636 of geometry on ice shelf ocean cavity ventilation: a laboratory experiment. *Experiments*
637 *in Fluids*, 55(5), 1-19.
- 638 Stern, A.A., Johnson, E., Holland, D.M., Wagner, T.J., Wadhams, P., Bates, R., Abra-
639 hamsen, E.P., Nicholls, K.W., Crawford, A., Gagnon, J. and Tremblay, J.E. (2015),
640 Wind-driven upwelling around grounded tabular icebergs. *J. of Geophys. Res.: Oceans*,
641 120(8), 5820-5835.

- 642 Stern, A. A., A. Adcroft, and O. Sergienko (2016), The effects of Antarctic iceberg calv-
643 ing?size distribution in a global climate model. *J. of Geophys. Res.: Oceans*, 121(8),
644 5773-5788.
- 645 Stern, A. A., A. Adcroft, O. Sergienko, G. Marques, R. Hallberg (2017), Modeling tabular
646 icebergs coupled to an ocean model. *Ocean Modeling*
- 647 Swope, W. C., H. C. Andersen, P. H. Berens, and K. R. Wilson (1982), A computer
648 simulation method for the calculation of equilibrium constants for the formation of
649 physical clusters of molecules: Application to small water clusters. *The Journal of
Chemical Physics* 76, no. 1, 637-649.
- 651 Tournadre, J., N. Bouhier, F. Girard-Ardhuin, and F. Rmy (2016), Antarctic icebergs
652 distributions 1992-2014. *J. Geophys Res: Oceans*.
- 653 Vernet, M., et al. (2012), Islands of ice: Influence of free-drifting Antarctic icebergs on
654 pelagic marine ecosystems, *Oceanography*, 25(3), 3839
- 655 Weeks, W. F., and W. J. Campbell (1973). Icebergs as a fresh-water source: an appraisal.
656 *J. of Glaciol.*, 12(65), 207-233.
- 657 White, L., A. Adcroft, and R. Hallberg (2009), High-order regriddingremapping schemes
658 for continuous isopycnal and generalized coordinates in ocean models. *J. of Comp.
Phys.*, 228(23), 8665-8692.

8. Supplementary material

660 This must be moved to its own document.

8.1. Static ice-shelf simulation

661 The results in the Lagrangian static ice-shelf simulation fit within the current under-
662 standing of ice-shelf cavity circulations based on ice-shelf observations [MacAyeal , 1984;
663 Lewis and Perkin , 1986; Jacobs et al , 2011] and previous modeling efforts [Determan and
664 Gerdes , 1994; Holland and Feltham , 2006; Losch , 2008]. The ocean temperatures inside
665 the domain are warmer than the in-situ freezing point (Figure S3a), and cause melting
666 at the ice-shelf base (Figure S4a). The meltwater entering the domain is more buoyant
667 than the water around it, and rises along the ice shelf as a cool fresh plume (Figure
668 S3b,c). This injection of positive buoyancy at depth drives a clockwise circulation outside
669 of the ice-shelf cavity (Figure 4a), providing the ice-shelf cavity with a continuous supply
670 of warm water, which provides the thermal energy required for continuous ice-shelf melt.
671 Strong meridional jets are observed at the ice front along the flanks of the domain, fluxing
672 water into the ice-shelf cavity on the eastern flank and allowing water to leave the ice-shelf
673 cavity on the western side (Figure 4a). The meridional flow in the center of the ice front
674 is much smaller, consistent with the dynamical barrier at the ice shelf front discussed in
675 previous modeling and experimental studies [Holland and Jenkins , 2001; Stern et al ,
676 2014].

677 The highest melt rates are observed within 100km of the grounding line (Figure S4a).
678 These elevated melt rates are caused by the presence of warm water (Figure S4b) and
679 increased ocean velocities (Figure S4c) near the grounding line, as well as the fact that
680 freezing point of ice decreases with increasing pressure. Elevated melt rates are also seen

681 near the ice front, caused by strong currents running along the ice-shelf front (Figure S4c).

682

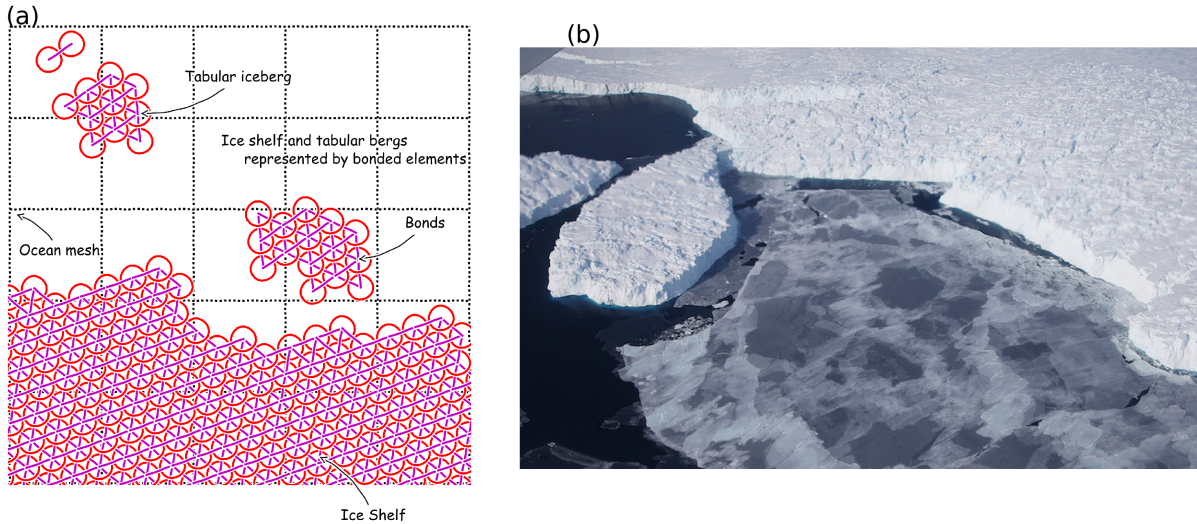


Figure 1. Schematic showing how ice shelves and tabular icebergs are constructed using Lagrangian elements. (a) Schematic of multiple ice elements that are joined together by numerical bonds (magenta lines) to form larger structures such as ice shelves and tabular icebergs. These numerical elements have finite extent and are able to interact with the ocean across multiple grid cells, and can interact with other elements. (b) Areal photograph of an ice shelf and tabular iceberg with elements superimposed over it to illustrate how the Lagrangian elements can be used to model ice shelves and tabular icebergs. In this schematic the ice elements (purple dots) are initialized in a staggered lattice covering the surface area of the iceberg. For the purpose of mass aggregation, the ice elements are assumed to have hexagonal shape (red hexagons). For the purpose of element interactions, the ice elements are assumed to be circular (black circles). Elements are initially bonded to adjacent elements using numerical bonds (magenta lines). These numerical bonds form equilateral triangles which give the shape rigidity. An ocean grid has been included (dashed cyan lines). Still need to update this figure to include the super imposed hexagons. Also, perhaps we want to remove some of the text in the caption? (e.g.: remove from the words "In this schematic the ice elements").

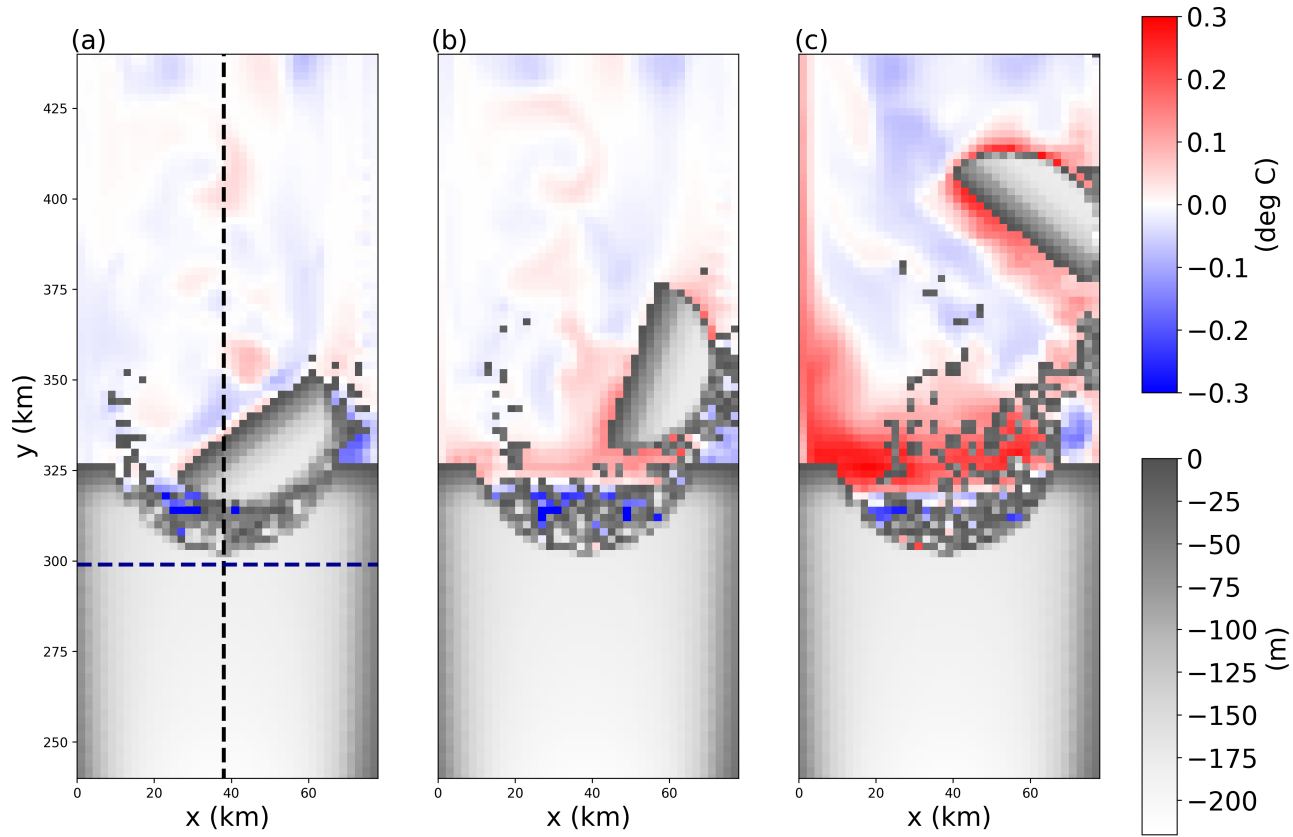


Figure 2. Snapshots of sea surface temperature anomalies in the iceberg-calving simulation.

The anomalies are relative to pre-calving temperatures. Snapshots are taken (a) 7, (b) 15, and (c) 50 days after calving. Grid cells with ice mass $> 10^4$ kg are plotted in white, with grey shading indicating thinner ice. The black and blue dashed line in panel (a) shows the location of the vertical transects shown in Figures 6 and 9, and 7 and 13, respectively.

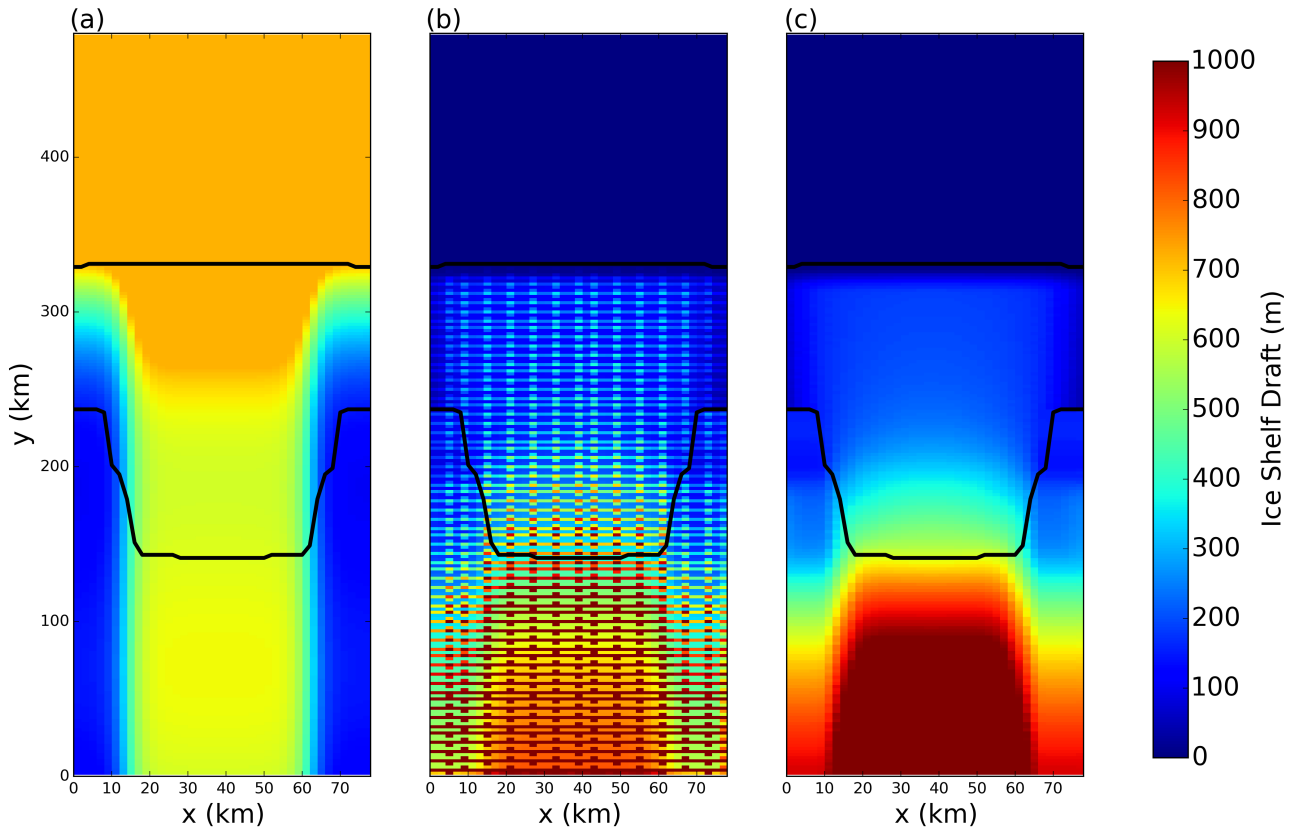


Figure 3. (a) Ocean bottom topography and (c) ice-shelf draft used to initialized the static ice shelf experiment simulation. The ice draft is calculated from the total mass of ice intersecting each ocean grid cell (see Section 2.6). Panel (b) shows the initial ice draft that would be calculated if the mass aggregation onto the Eulerian grid was not used (i.e. elements treated as point masses). The lower and upper black lines denote the grounding line and ice shelf front, respectively. This figure is reproduced from [Stern et al., 2017].

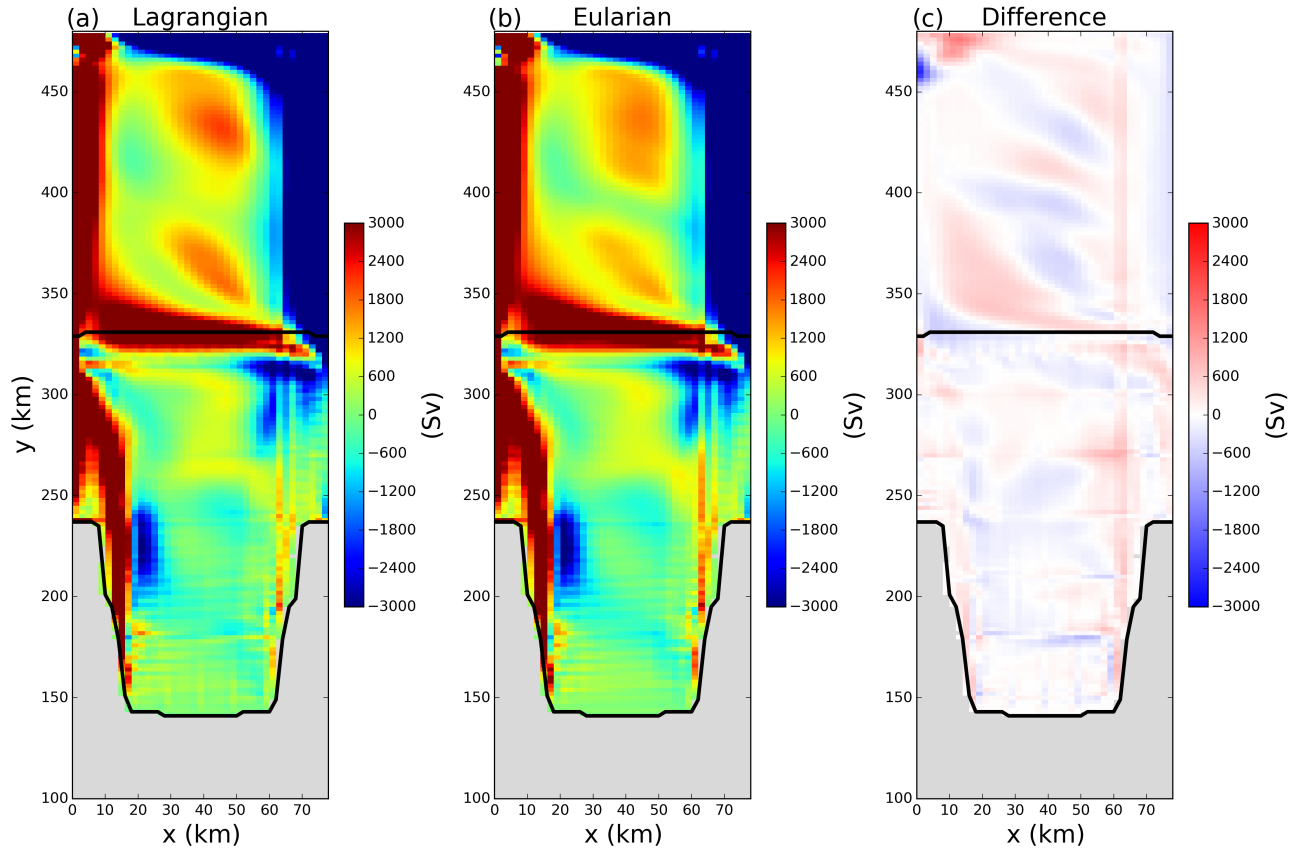


Figure 4. Time-averaged barotropic stream function in the (a) Lagrangian and (b) Eulerian simulations in the static ice-shelf configuration. Panel (c) shows the difference between panels (a) and (b). The time averages are taken over 5 years of model time, beginning at the end of the 5 year spin up period. **Something is wrong with the units in this figure**

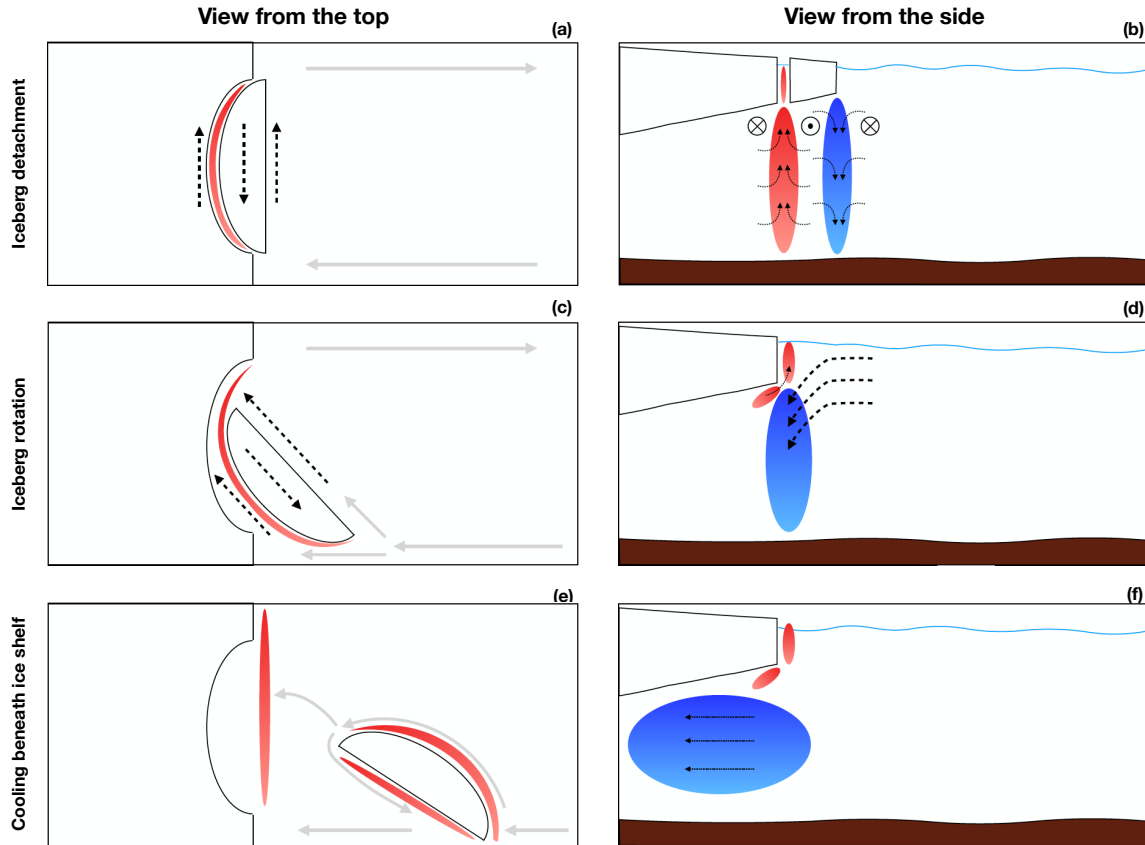


Figure 5. Schematic illustrating how the ocean hydrography is affected by iceberg calving. Cool and warm water anomalies are indicated in blue and red, respectively, and ocean currents are shown using arrows.

Stage 1, iceberg detachment (a, b): as the iceberg detaches, water column stretching behind the iceberg causes warm water anomalies behind the iceberg. The conservation of PV caused by this stretching gives rise to a pair zonal jets behind and below the iceberg. Similarly, the contracting water column in front of the iceberg creates cool anomalies, and drives a zonal jet in front and below the iceberg.

Stage 2, iceberg rotation (c, d): as the iceberg drifts away from the ice shelf, it rotates causing the jets around it to change direction. The newly orientated jet in front of the iceberg drives water towards the ice shelf, which subducts at the ice front, causing subsurface cooling.

Stage 3, cooling below the ice shelf (e, f): as the iceberg moves away from the ice shelf, it interacts with the boundary currents, which are diverted by the presence of the iceberg. At the ice front, the cool water anomalies are advected into the ice-shelf cavity, eventually leading to reduced melt rates throughout the cavity.

The warm water surface anomalies behind the iceberg after calving (panel a), move with the iceberg as it drifts (panel b), and entirely surround the iceberg as it continues to drift into the open ocean (panel c).

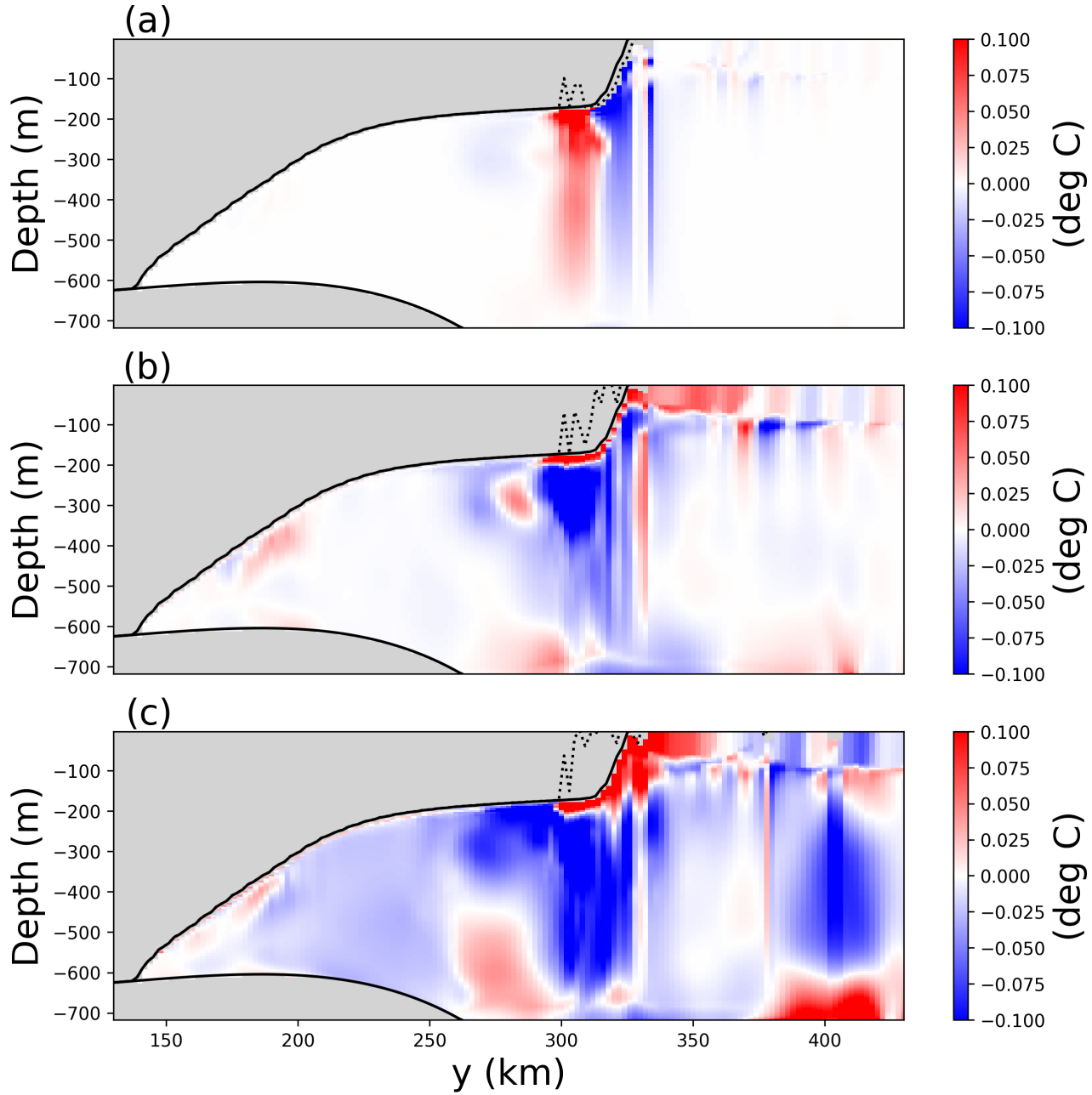


Figure 6. Snapshots of vertical sections of ocean temperature anomaly at $x=40$ km in the iceberg-calving experiment. The anomalies are relative to pre-calving temperatures. Snapshots are taken (a) 1, (b) 15, and (c) 50 days after calving. In each panel, the base of the ice before calving and at the time of the snapshot are shown by the solid and dashed black lines, respectively. Positions that were not the ocean interior at in both snapshots are masked in grey. The position of the vertical transects is shown by the black dashed lines in Figure 2a.

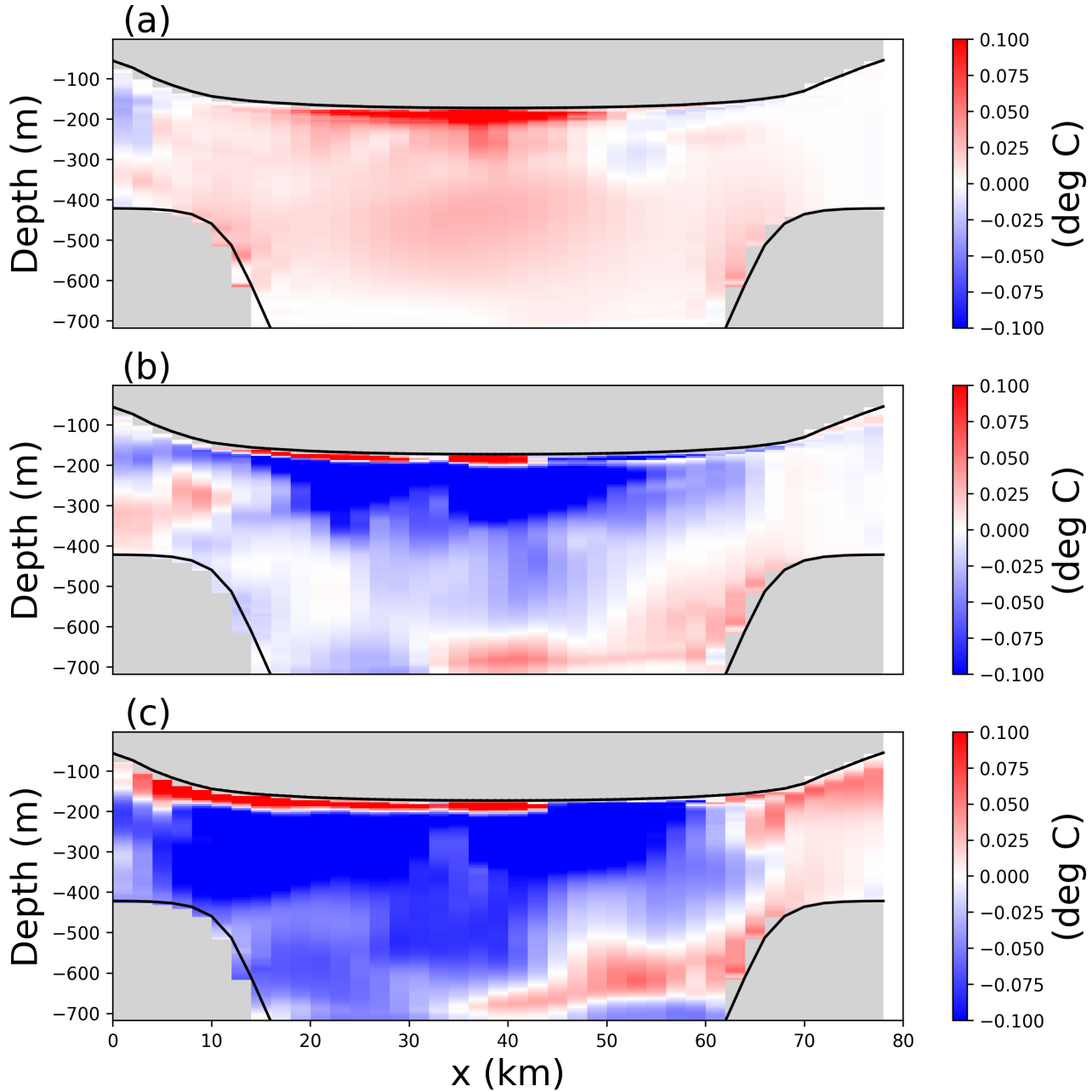


Figure 7. Snapshots of vertical sections of ocean temperature anomaly at $y=300$ km in the tabular-iceberg-calving experiment. The anomalies are relative to pre-calving temperatures. Snapshots are taken (a) 1, (b) 15, and (c) 50 days after calving. The position of the vertical transects is shown by the blue dashed lines in Figure 2a.

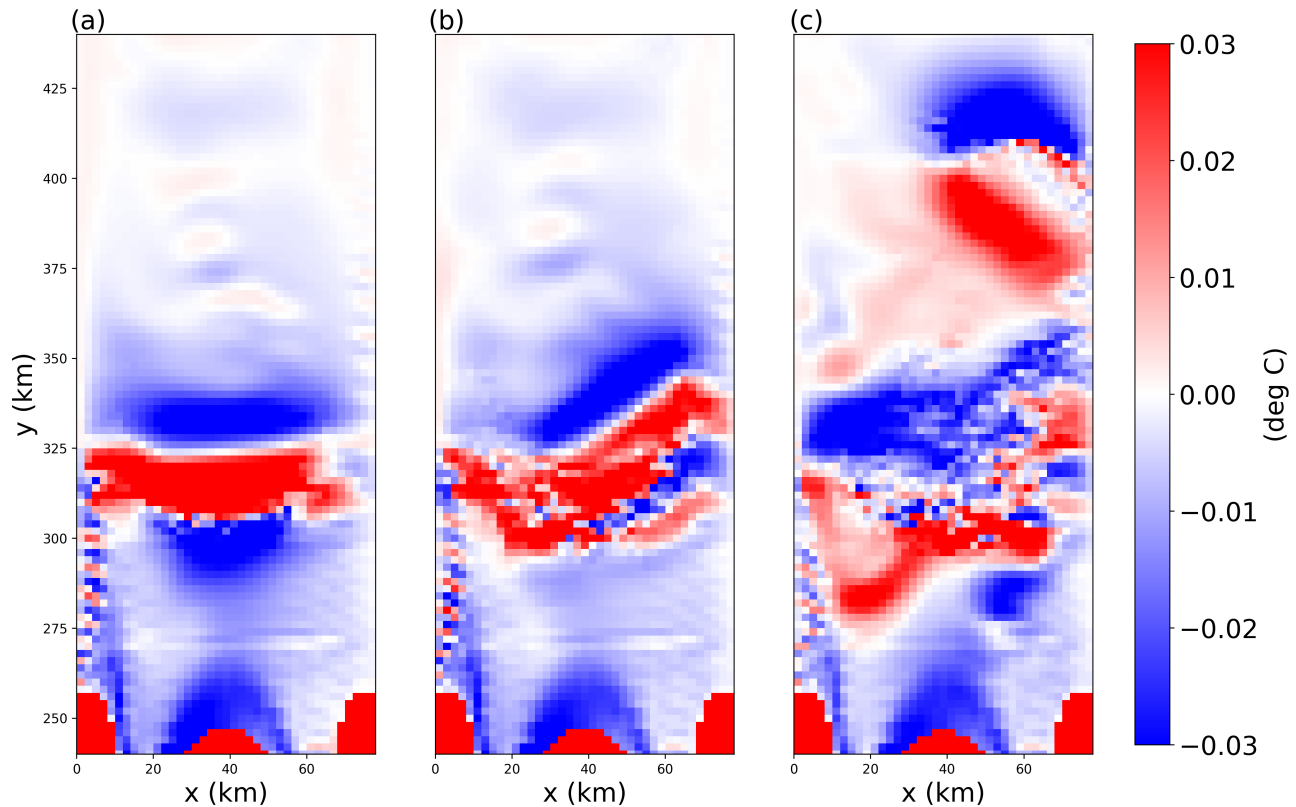


Figure 8. Snapshots of ocean zonal velocity at $z=197.5$ m(?) in the iceberg-calving experiment.

Snapshots are taken (a) 1, (b) 15, and (c) 50 days after calving. I should include an outline of the iceberg shape in this figure

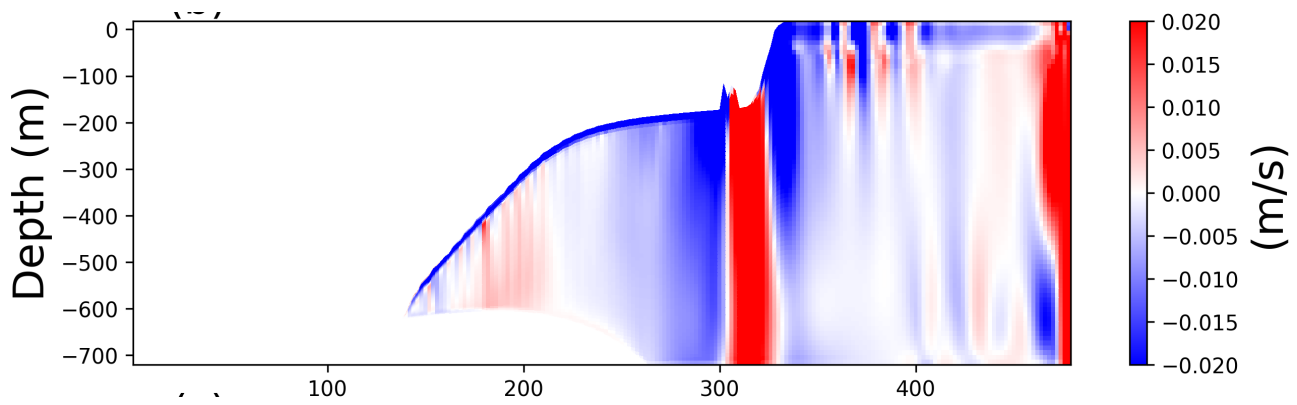


Figure 9. Snapshot of vertical section of zonal velocity at $x=40$ km in the iceberg-calving experiment 1 day after calving. The position of the vertical transects is shown by the black dashed line in Figure 2a. An eastward jet is observed beneath the iceberg, and westward jets are observed to the north and south of the iceberg.

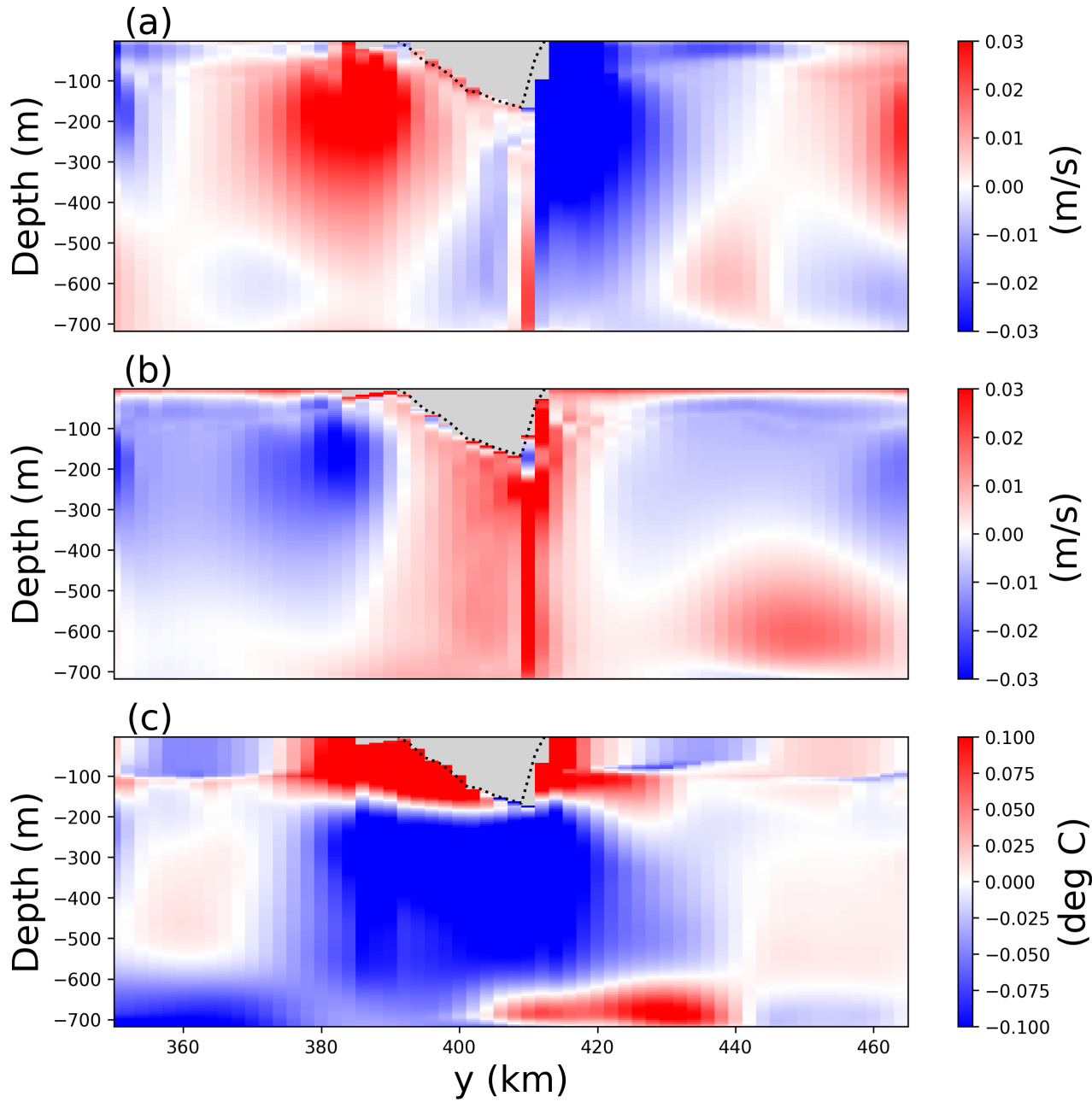


Figure 10. Snapshots of vertical sections of ocean (a) zonal velocity, (b) meridional velocity, and (c) temperature anomaly at $x=60$ km in the tabular-iceberg-calving experiment. The anomalies are relative to pre-calving temperatures. Snapshots are taken 50 days after calving.

Should we add the position to Figure 2a?

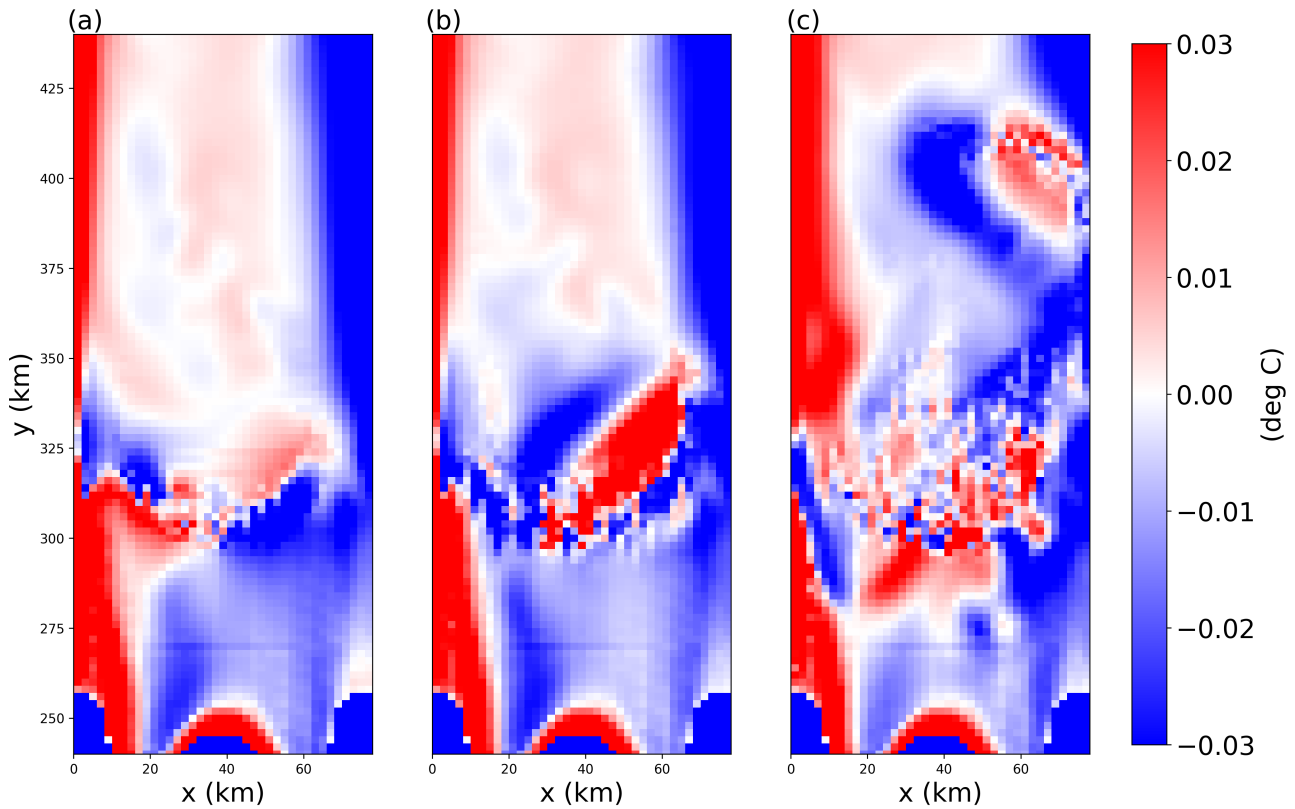


Figure 11. Snapshots of ocean meridional velocity at $z=197.5$ m in the iceberg-calving experiment. Snapshots are taken (a) 1, (b) 15, and (c) 50 days after calving. I should include an outline of the iceberg shape in this figure

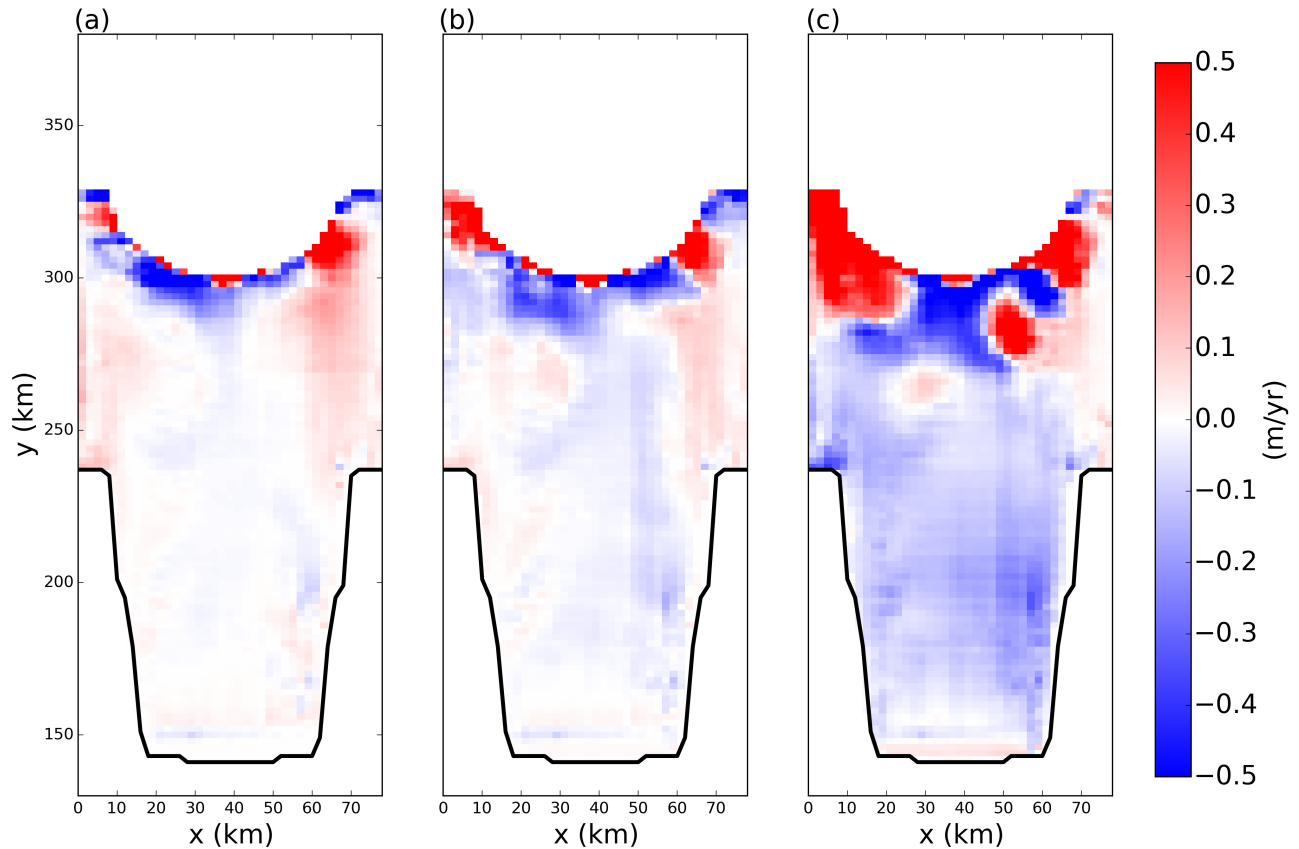


Figure 12. Snapshots of the melt rate anomaly, at the ice-shelf base in the tabular iceberg-calving simulation. The anomalies are relative to pre-calving melt rates. Snapshots are taken (a) 7, (b) 15, and (c) 50 days after calving.

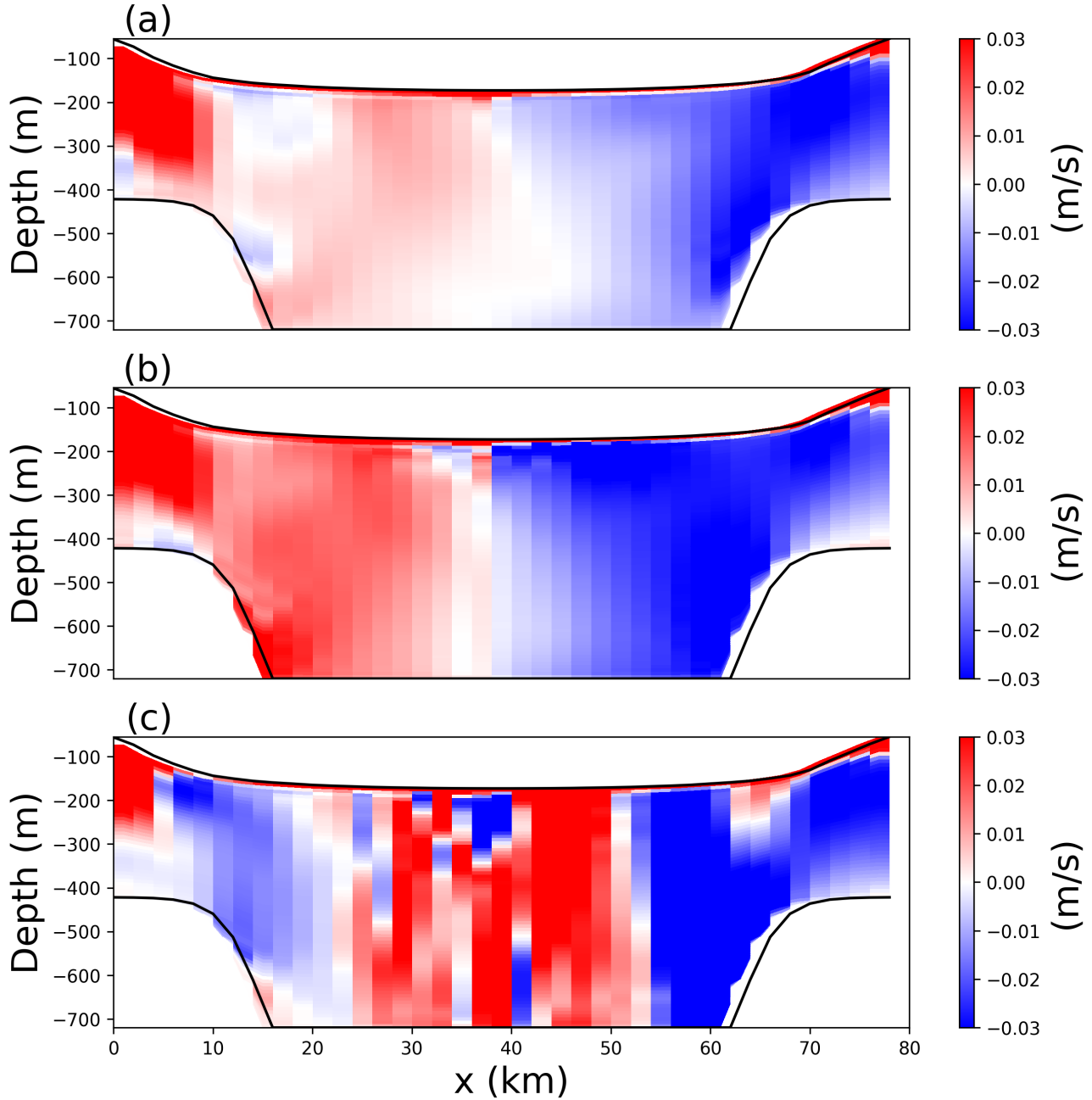


Figure 13. Snapshots of vertical sections of meridional velocity at $y=300$ km in the tabular-iceberg-calving experiment. Snapshots are taken (a) 0, (b) 1, and (c) 50 days after calving. The position of the vertical transects is shown by the blue dashed lines in Figure 2a. Could show 1,14 and 50 days after calving to be consistent with the other Figures. But this figure is more interesting

Parameter	Symbol	Value	Unit
Domain Length	L_x	80	km
Domain Width	L_y	480	km
Horizontal Resolution	Δx	2	km
Number of vertical layers	N_l	72	non-dim
Horizontal Viscosity	ν_H	6.0	$\frac{m^2}{s}$
Diapycnal Viscosity	ν_V	10^{-3}	$\frac{m^2}{s}$
Horizontal Diffusivity	ϵ_H	1.0	$\frac{m^2}{s}$
Diapycnal Diffusivity	ϵ_V	5×10^{-5}	$\frac{m^2}{s}$
Initial Surface Temperature	T_t	-1.9	$^{\circ}C$
Initial Bottom Temperature	T_b	1.0	$^{\circ}C$
Initial Surface Salinity	S_t	33.8	psu
Initial Bottom Salinity	S_b	34.7	psu
Maximum Ocean depth	H_{ocean}	720	m
Relaxation Time of Sponge Layer	T_{sponge}	0.1	days
Time Step for Static Shelf Experiment	dt_{Static}	1000	s
Time Step for Iceberg Calving Experiment	$dt_{Calving}$	10	s

9. Supplementary Figures

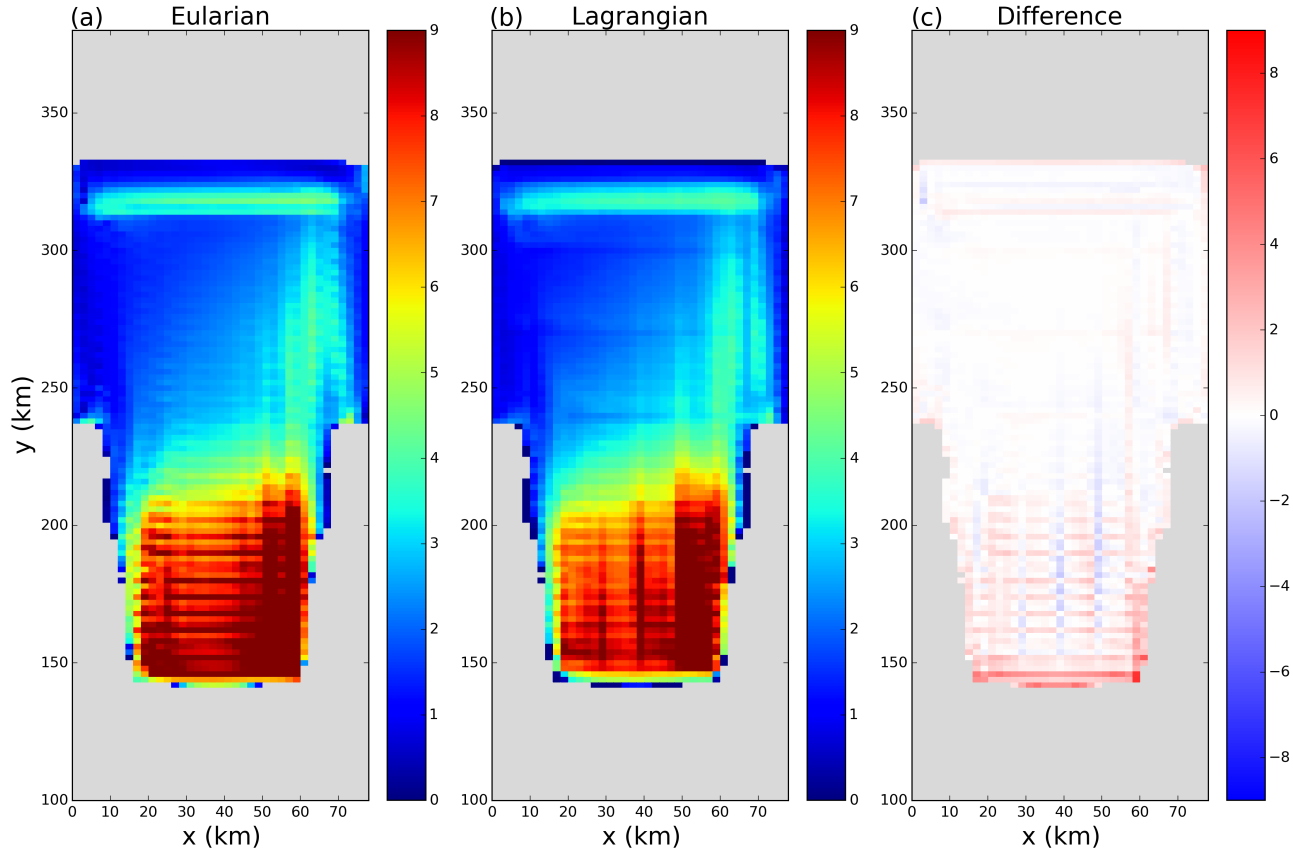


Figure S1. Time-averaged melt rates in the (a) Lagrangian and (b) Eulerian simulations in the static ice-shelf configuration. Panel (c) shows the difference between panels (a) and (b). The time averages are taken over 5 years of model time, beginning at the end of the 5 year spin up period.

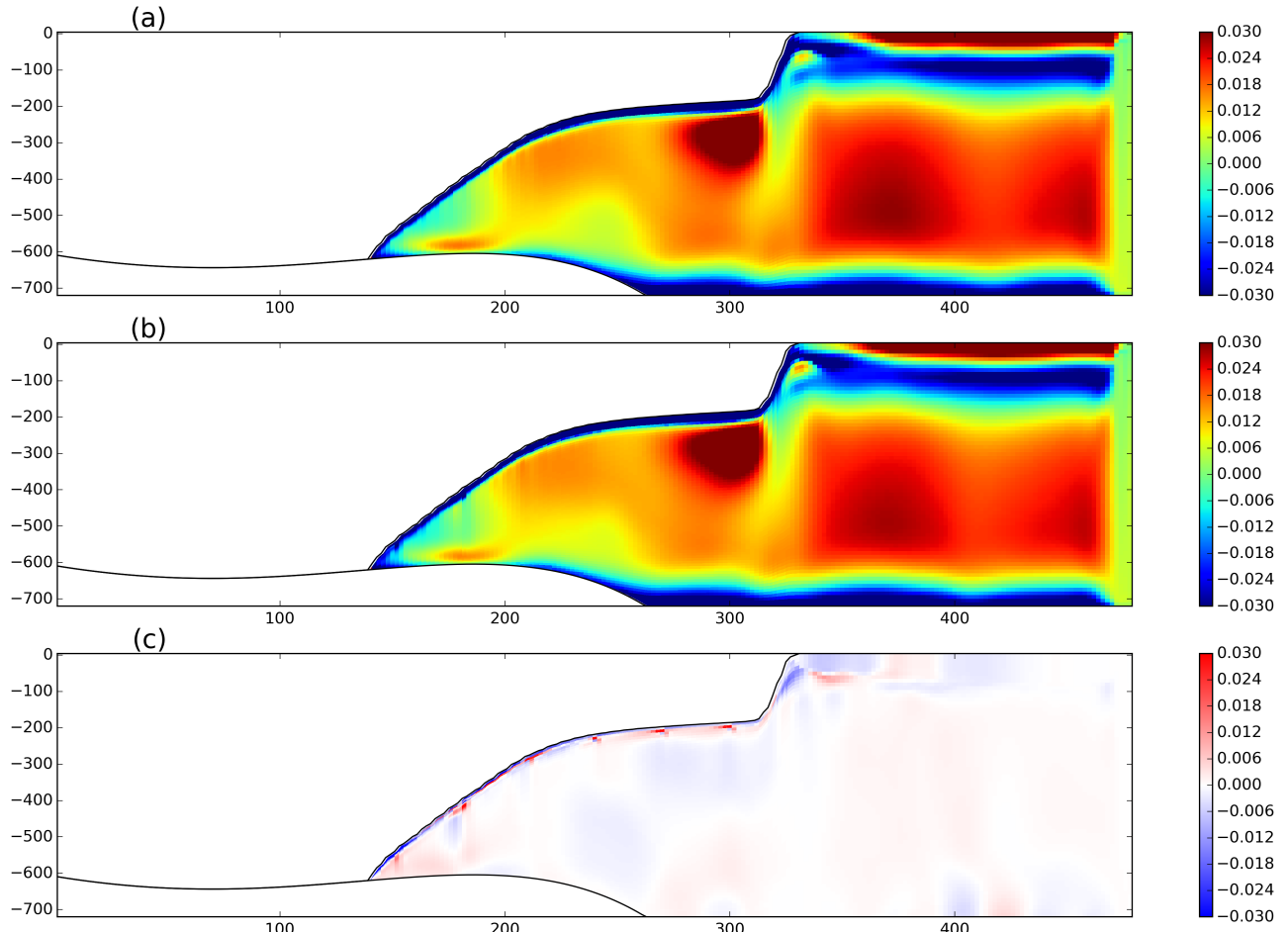


Figure S2. Time-averaged vertical sections of salinity at $x = 40$ km in the (a) Lagrangian and (b) Eulerian simulations in the static ice-shelf configuration. Panel (c) shows the difference between panels (a) and (b). The time averages are taken over 5 years of model time, beginning at the end of the 5 year spin up period. The position of the vertical transects is shown by the black dashed lines in Figure 2a.

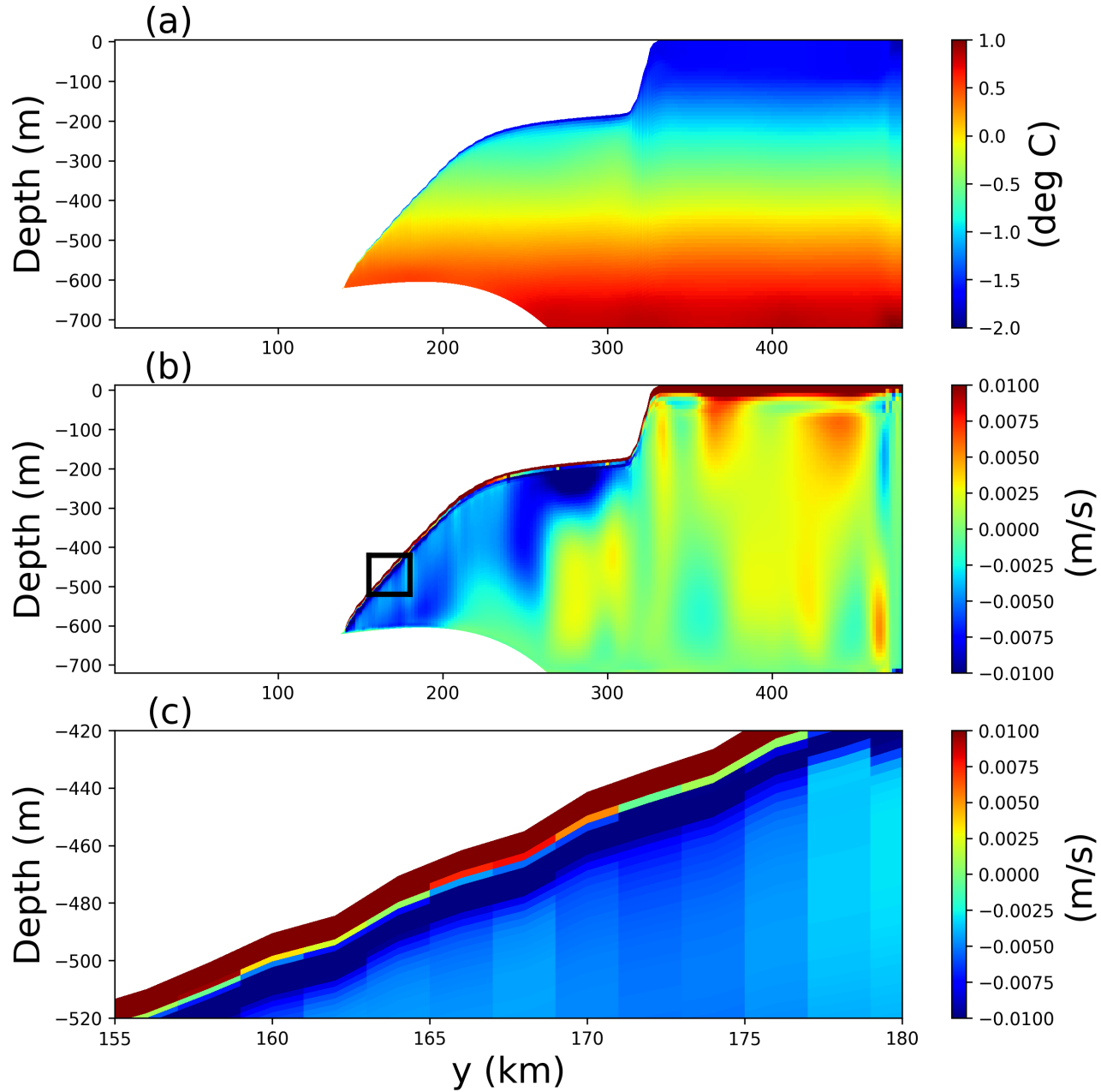


Figure S3. Snapshots of the static ice-shelf experiment taken after 5 years of model simulation, using the Lagrangian ice-shelf model coupled to the MOM6 ocean model. Panels show cross sections of the (a) the steady-state ocean temperature, and (b) the meridional ocean velocity. Panel (c) again shows the meridional ocean velocity, and is zoomed into the region near the ice-shelf base (the zoomed-in region is indicated with a black box (b)).

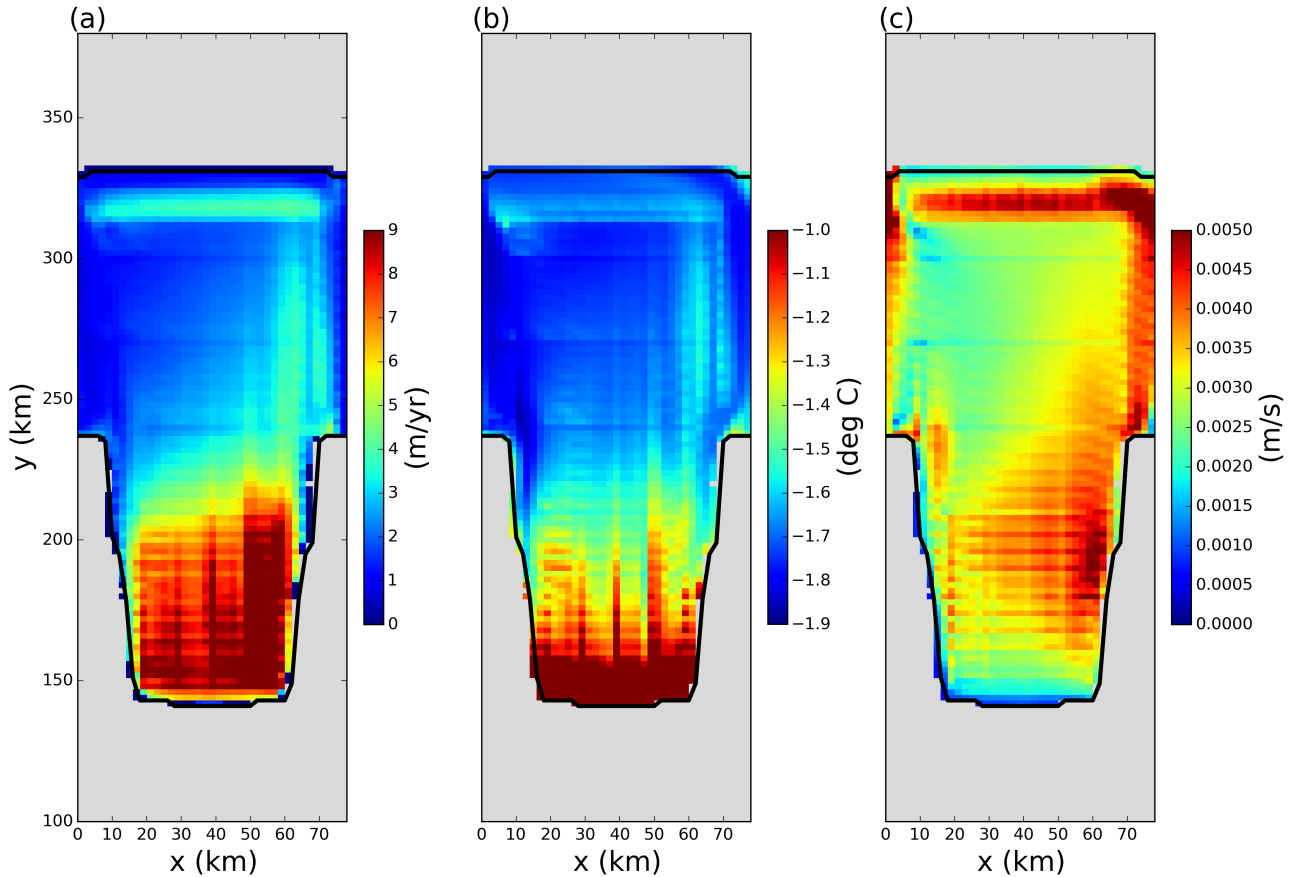


Figure S4. Results of the static ice-shelf experiment using the Lagrangian ice-shelf model coupled to MOM6. The three panels show 5 year time average of the (a) melt rate, (b) top-of-ocean temperature and (c) frictional velocity, u^* , at the base of the ice shelf. Fields are only shown in regions where the ice area fraction is ≥ 0.8 .

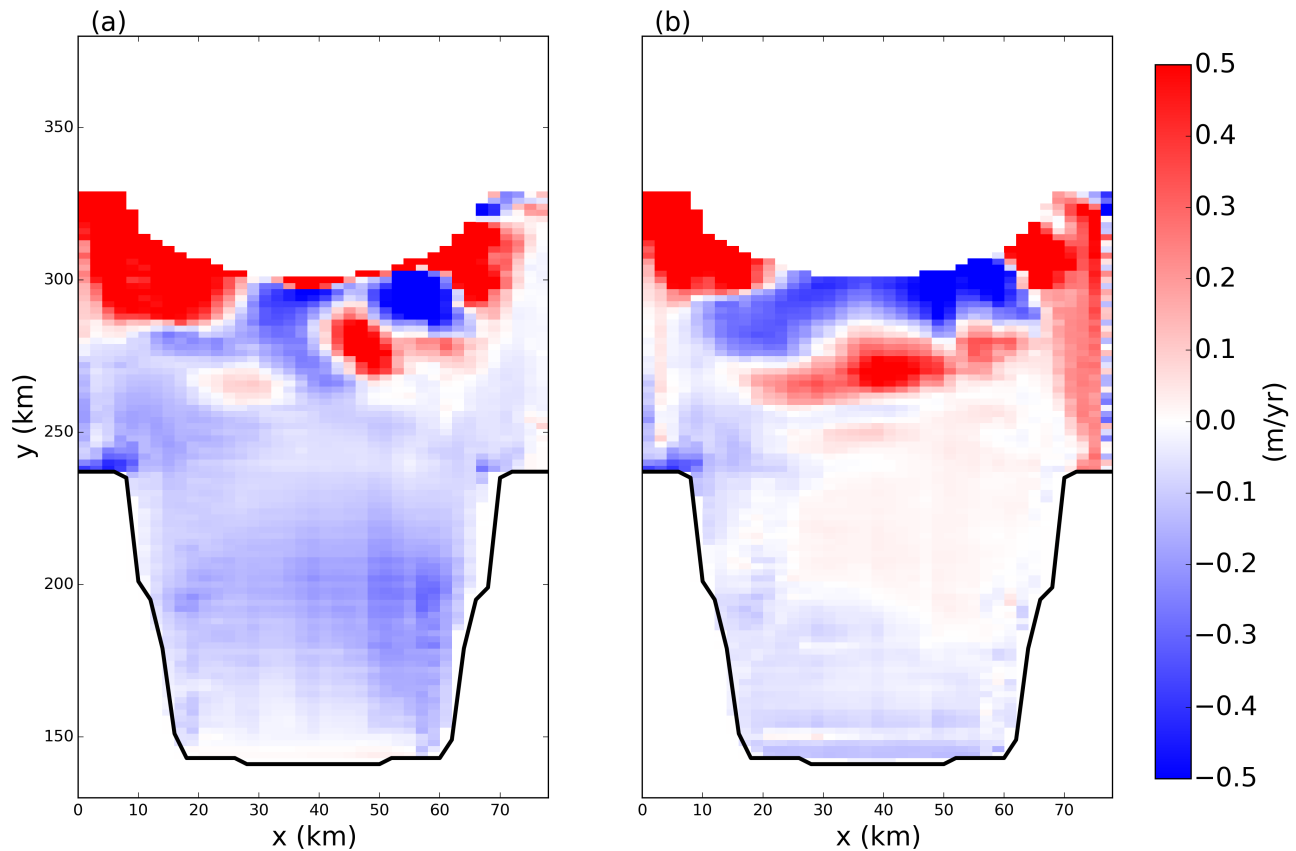


Figure S5. (a) Snapshot of the melt rate at the base of the ice shelf 60 days after the calving event in the tabular-iceberg-calving simulation. (b) Steady state melt rate of the simulation that was spun-up from rest with the semi-circular iceberg removed..

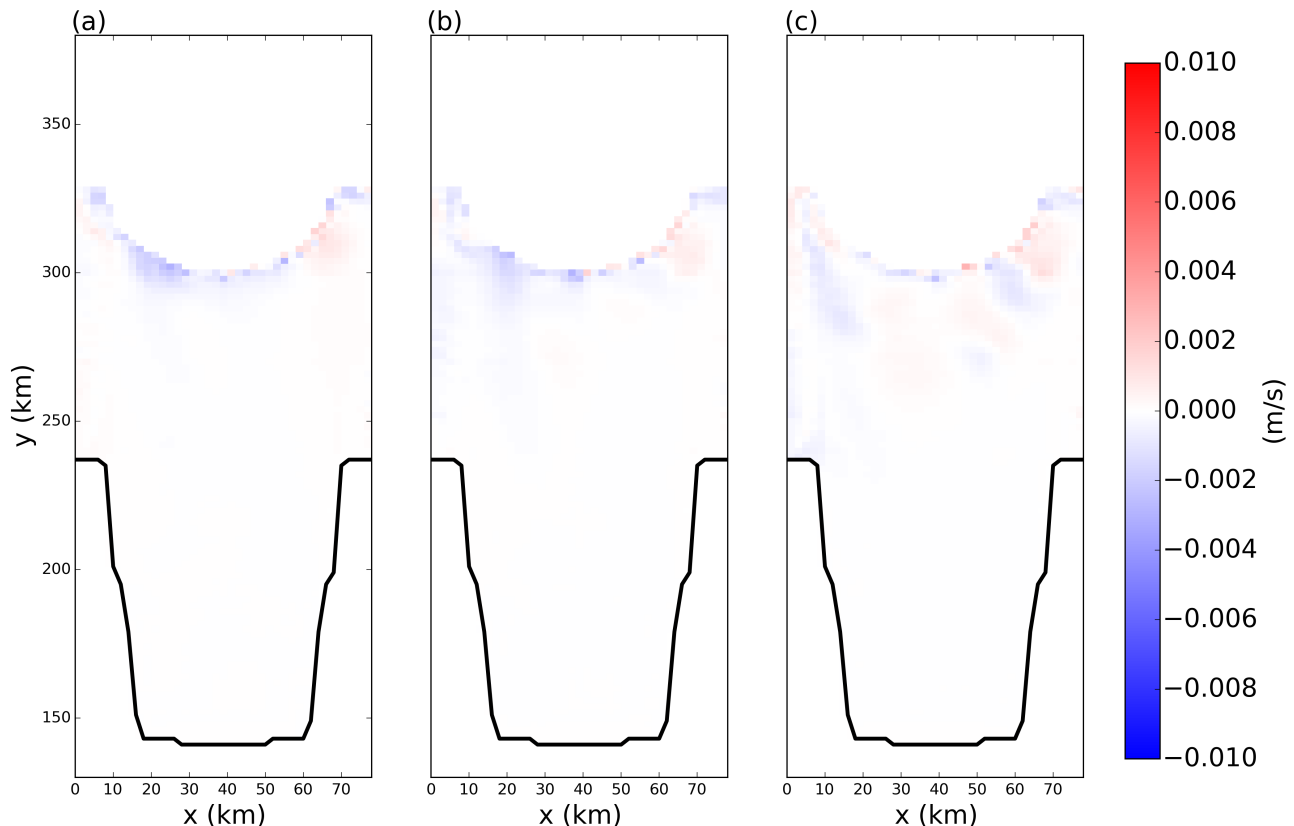


Figure S6. Snapshots of frictional velocity at the ice-shelf base in the tabular-iceberg-calving simulation. Snapshots are taken (a) 7, (b) 15, and (c) 50 days after calving.

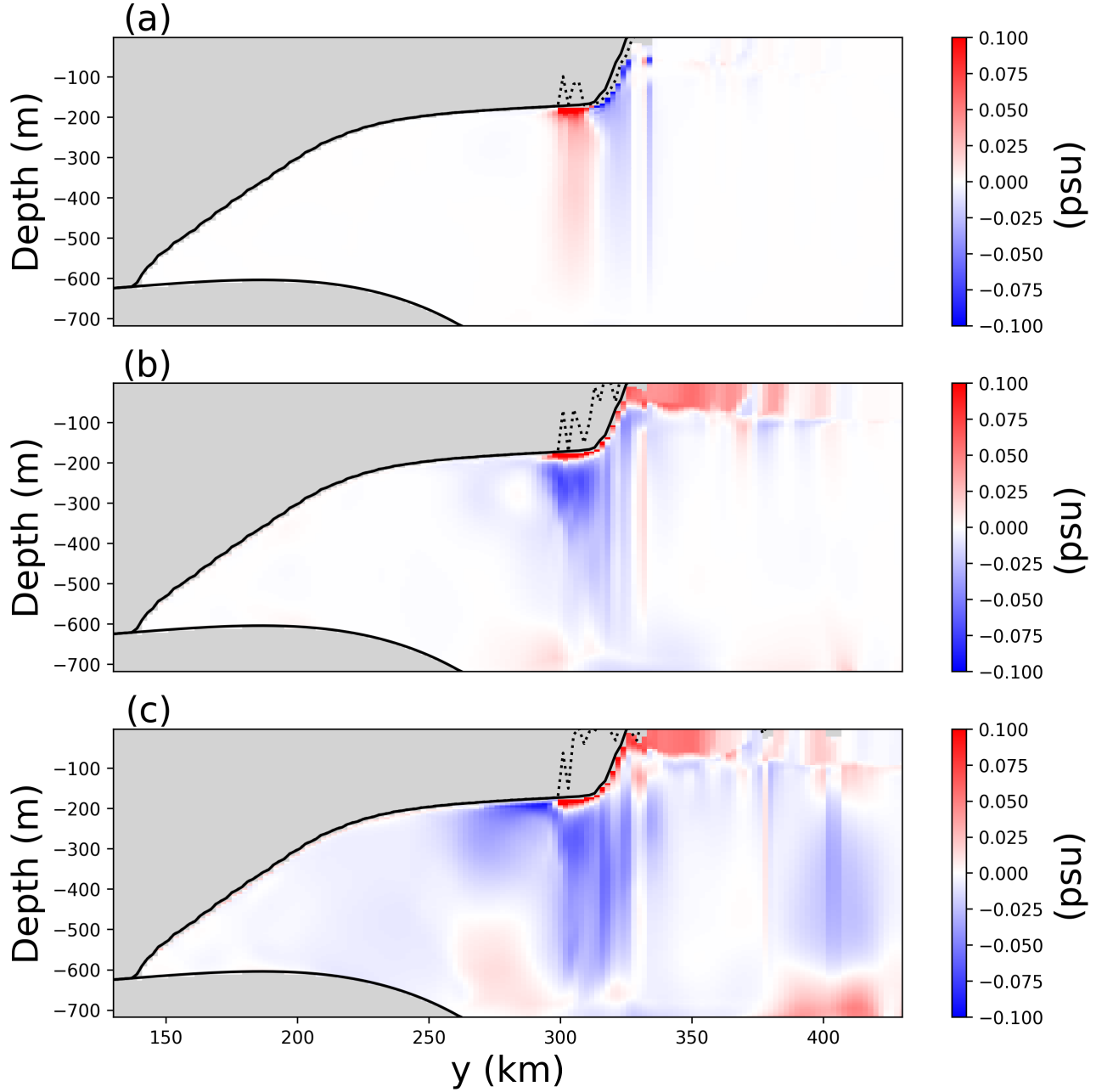


Figure S7. Snapshots of vertical sections of ocean salinity anomaly at $x=40$ km in the iceberg-calving experiment. The anomalies are relative to pre-calving temperatures. Snapshots are taken (a) 1, (b) 15, and (c) 50 days after calving. In each panel, the base of the ice before calving and at the time of the snapshot are shown by the solid and dashed black lines, respectively. Positions that were not the ocean interior at in both snapshots are masked in grey. The position of the vertical transects is shown by the black dashed lines in Figure 2a.